Title

Impacts of an ethanol-blended fuel release on groundwater and fate of produced methane: Simulation of field observations

Journal

Water Resources Research, 49(8)

ISSN

0043-1397

Authors

Rasa, Ehsan
Bekins, Barbara A
Mackay, Douglas M
et al.

Publication Date

2013-08-01

DOI

10.1002/wrcr.20382

Peer reviewed

Published in final edited form as:
Water Resour Res. 2013 August ; 49(8): 4907–4926. doi:10.1002/wrcr.20382.

Impacts of an ethanol-blended fuel release on groundwater and fate of produced methane: Simulation of field observations

Ehsan Rasa,
Department of Civil and Environmental Engineering, University of California-Davis, One shield Avenue, Davis, California, 95616, USA. Phone: +1-530-574-8193. erasa@ucdavis.edu

Barbara A. Bekins,
U.S. Geological Survey, 345 Middlefield Rd, Menlo Park, California, 94025, USA. Phone: +1-650-329-4691. babekins@usgs.gov

Douglas M. Mackay,
Department of Land, Air, and Water Resources, University of California-Davis, One shield Avenue, Davis, California, 95616, USA. Phone: +1-650-324-2809. dmmackay@ucdavis.edu

Nicholas R. de Sieyes,
Department of Land, Air, and Water Resources, University of California-Davis, One shield Avenue, Davis, California, 95616, USA. Phone: +1-805-403-6820. nrdesieyes@ucdavis.edu

John T. Wilson,
U. S. Environmental Protection Agency, Ada, Oklahoma 74820, USA. Phone: +1-580-436-8534. Wilson.JohnT@epamail.epa.gov

Kevin P. Feris,
Department of Biology, Boise State University, Boise, Idaho 83725, USA. Phone: +1-208-426-5498. kevinferis@boisestate.edu

Isaac A. Wood, and
CH2M-Hill consultants, 150 Spear Street, Suite 750, San Francisco, CA, 94105, USA. Phone: +1-415-728-0650. isaac.wood@ch2m.com

Kate M. Scow
Department of Land, Air, and Water Resources, University of California-Davis, One shield Avenue, Davis, California, 95616, USA. Phone: +1-530-752-4632. kmscow@ucdavis.edu

Abstract

In a field experiment at Vandenberg Air Force Base (VAFB) designed to mimic the impact of a small-volume release of E10 (10% ethanol and 90% conventional gasoline), two plumes were created by injecting extracted groundwater spiked with benzene, toluene, and *o*-xylene, abbreviated BT*o*X (No-Ethanol Lane) and BT*o*X plus ethanol (With-Ethanol Lane) for 283 days. We developed a reactive transport model to understand processes controlling the fate of ethanol and BT*o*X. The model was calibrated to the extensive field dataset and accounted for concentrations of sulfate, iron, acetate, and methane along with iron-reducing bacteria, sulfate-reducing bacteria, fermentative bacteria, and methanogenic archaea. The benzene plume was about 4.5 times longer in the With-Ethanol Lane than in the No-Ethanol Lane. Matching this different behavior in the two lanes required inhibiting benzene degradation in the presence of ethanol. Inclusion of iron reduction with negligible growth of iron-reducers was required to reproduce the

Correspondence to: Ehsan Rasa.
Ehsan Rasa, Now at Geosyntec Consultants, 1111 Broadway, Oakland, California, 94607, USA.

observed constant degradation rate of benzene. Modeling suggested that vertical dispersion and diffusion of sulfate from an adjacent aquitard were important sources of sulfate in the aquifer. Matching of methane data required incorporating initial fermentation of ethanol to acetate, methane loss by outgassing, and methane oxidation coupled to sulfate and iron reduction. Simulation of microbial growth using dual Monod kinetics, and including inhibition by more favorable electron acceptors, generally resulted in reasonable yields for microbial growth of 0.01-0.05.

Keywords

Ethanol; BTEX; anaerobic; methanogenic; reactive transport

1. Introduction

Ethanol has been increasingly used as a gasoline additive to lower greenhouse emissions and expand the use of biofuels [*ITRC*, 2011]. A great deal of research has recently been focused on assessing and predicting the impacts of ethanol on the biodegradation of benzene, toluene, ethylbenzene, and xylenes (BTEX) at gasohol spill sites [e.g., *Powers et al*., 2001; *Mackay et al*., 2006; *Spalding et al*., 2011]. Because ethanol is a labile electron donor readily consumed by microorganisms, laboratory, field, and numerical studies have identified a number of key geochemical and microbiological features of such spills. *Powers et al*. [2001] summarized the important processes including depletion of electron acceptors, changes in microbial populations, and production of methane. Although our understanding of ethanol fate and impacts in the subsurface has improved recently, no study to date has conducted detailed, transient numerical simulations incorporating all of the key processes.

The ability of spilled ethanol to quickly drive groundwater systems anaerobic and potentially impact gasoline product degradation has been illustrated in a number of studies [*Chen et al*., 2008; *Corseuil et al*., 1998; *Corseuil et al*., 2011; *Deeb et al*., 2002; *Mackay et al*., 2006]. In laboratory microcosm experiments conducted by Corseuil et al. [1998], anaerobic conditions quickly developed in aquifer sediments when ethanol was present and significantly retarded BTEX biodegradation rates compared to aerobic microcosms. *Deeb et al*. [2002] performed laboratory studies using a pure culture indigenous to a gasoline-contaminated aquifer and concluded that the biodegradation of 25 mg/L benzene in groundwater was highly inhibited in the presence of 25 mg/L ethanol. They suggested that benzene plume lengths can increase 16-34% in the presence of ethanol. In a field experiment, *Mackay et al*. [2006] studied the impact of ethanol on natural attenuation of benzene, toluene, and *o*-xylene (BT*o*X) under sulfate-reducing conditions in side-by-side injection experiments. They found that sulfate was substantially depleted downgradient from an injection of ethanol and BT*o*X, creating a methanogenic/acetogenic zone in the area of sulfate depletion. Biodegradation rates for BT*o*X in the ethanol-impacted lane were significantly slower than in the ethanol-free control. *Chen et al*. [2008] conducted a microcosm study under anaerobic conditions and reported that presence of intermediate degradation products of ethanol such as acetate, propionate and butyrate can create more reducing conditions and slow down benzene degradation. An ethanol-blended gasoline release experiment by *Corseuil et al*. [2011] showed ethanol degradation under methanogenic conditions while acetate accumulated and inhibited benzene degradation. Together these studies indicate the need for models of ethanol spills that include the effects of sequential use and depletion of terminal electron acceptors.

Ethanol has the potential to spur microbial growth in shallow groundwater [*Cápiro et al*., 2008; *Feris et al*., 2008; *Lovanh et al*., 2002; *Nelson et al*., 2010]. Low ethanol

concentrations (1 mg/L) supported biomass growth and increased biomass concentration by a factor of three during an experiment by *Lovanh et al*. [2002]. In a study by *Cápiro et al*. [2008] the response of microbial communities to a release of neat ethanol was measured using quantitative polymerase chain reaction (qPCR) analyses. They reported bacteria and archaea growth and methane production in shallow groundwater and soil samples. In a controlled ethanol release experiment, *Feris et al*. [2008] reported significant ethanol impacts on the ecology of bacteria, archaea, and sulfate-reducing bacteria (SRB). Results of *Feris et al*. [2008] showed that the apparent reduction in natural attenuation rates of BT*o*X in the presence of dissolved ethanol is due a combination of altered geochemistry and microbial community structure and function, including shifts in the bacterial and archaeal communities, and significant increases in putative methanogenic archaeal populations. These studies indicate that models of ethanol biodegradation should account for microbial growth and population shifts.

When the supply of ethanol exceeds what can be degraded using available electron acceptors, ethanol degradation can occur under methanogenesis and produce substantial amounts of methane and organic acids [*Freitas et al*., 2010; *Ma et al*., 2012; *Nelson et al*., 2010; *Spalding et al*., 2011; *Suflita and Mormile*, 1993]. In a microcosm study by *Suflita and Mormile* [1993] 50 mg/L ethanol was completely degraded by methanogenesis after an acclimation period of 25-30 days. *Freitas et al*. [2010] used stable carbon isotopes to distinguish the methane origin between gasoline and ethanol biodegradation and showed that organic acids from ethanol biodegradation can persist in groundwater even 2 years after an ethanol spill. In a recent study, *Spalding et al*. [2011] studied the effect of a spill of more than 75,000 liters (20,000 gallons) of E95 (95% vol/vol ethanol) and showed that although no plume of ethanol was detected in groundwater underlying the spill, a plume of BTEX and methane (more than 10 mg/L) was generated. Their data suggested that the dissolved methane was degraded in groundwater during transport, promoting anaerobic conditions and benzene persistence. In contaminant plumes, production of methane above solubility has led to degassing of methane from the saturated zone (e.g., *Amos et al*., 2005; *Ma et al*., 2012). These results show that models of ethanol plumes must include production and fate of methane and organic acids.

Several researchers have conducted reactive transport modeling of ethanol in groundwater [*Freitas et al*., 2011; *Gomez et al*., 2008; *Molson et al*., 2002]. These models have explored one or more of the key processes linked to ethanol degradation listed above. *Gomez et al*. [2008] used MODFLOW and RT3D to simulate the impact of ethanol on benzene plume length in a saturated hydrogeologic setting with oxygen as the only dissolved electron acceptor. *Freitas et al*. [2011] used BIONAPL to simulate the mass discharge of BTEX compounds in groundwater during a field experiment where a residual source of ethanol-blended gasoline was emplaced below the water table. *Molson et al*. [2002] simulated NAPL dissolution and studied the effect of ethanol on the persistence of benzene in gasoline-contaminated aquifers under aerobic conditions. None of these studies included sequential electron acceptors or methane production and fate. The modeling study of *Gomez et al*. [2008] included microbial growth but did not compare the model results to field data.

The purpose of this study was to construct a conceptual and numerical model that includes each of the most important processes known to impact ethanol fate in the subsurface and reproduces key features of field data from an experimental ethanol release. For the purpose of this comparison, we used the dataset collected during the comprehensive controlled release field experiments at Vandenberg Air Force Base in 2004-2005 by *Mackay et al*. [2006]. The experimental design and major findings of that study are described below. An iterative process of calibration to field data followed by model refinement was used to improve the model beyond the base case, which allowed for identification of those

physicochemical processes most important for accurate representation of ethanol degradation and impact in the field.

2. Field experiment design and major findings

Site 60, Vandenberg Air Force Base (VAFB), California, (Fig. 1) has been described in detail previously (Mackay et al. 2012 and references cited therein). Within the 60-m-long study area, several thin, horizontal, sandy layers exist within 4 m of the ground surface and the sand layer denoted S3 (Fig. 2) is the primary groundwater aquifer. Details of the ethanol injection experiment in 2004-05 at VAFB are described in *Mackay et al*. [2006]. In brief, side-by-side experiments were conducted involving the injection of site groundwater spiked with selected BTEX species, with and without ethanol for 283 days. On the west side (No-Ethanol Lane), 200 mL/min of water was injected that had been spiked continuously with benzene (B), toluene (T), *o*-xylene (*o*X), and periodically with tracers; hereafter the selected BTEX species are abbreviated BT*o*X. On the east side (With-Ethanol Lane), the same flow rate of water was spiked continuously with ethanol plus the same concentrations of BT*o*X and periodically with tracers. Flow was split equally into three injection wells for each lane. The average injection concentrations were 2.3 mg/L for benzene, 2.2 mg/L for toluene, and 0.87 mg/L for *o*-xylene. In the With-Ethanol Lane the average ethanol injection concentration was 470 mg/L. The progress of the experiments was monitored with 192 monitoring wells with 0.91 m (3 feet) screens spanning the S3 aquifer (Fig. 1). Sampling events consisted of five major snapshots of the BT*o*X and ethanol (at 27, 64, 115, 206, and 274 days), one major snapshot of other analytes (acetate, propionate, butyrate, methane, nitrate, sulfate, DO, pH, and ferrous iron; at 170 days), and two snapshots of microbial populations in groundwater (at 152 and 244 days).

The average groundwater hydraulic gradient around the time of the experiment was 0.0132 and the mean groundwater flow velocity was estimated to be 0.42 m/day. Distributed groundwater recharge is considered negligible in this location and was not included in the model. Concentrations of background sulfate (the predominant dissolved electron acceptor in the groundwater at the site) averaged 120 mg/L. Analyses by *Wood* [2004] found that close to where the experimental plumes were created, the bioavailable ferric iron concentration in the aquifer sediments was 750-1,250 mg/kg. Other dissolved electron acceptors, including dissolved oxygen, were negligible or not detectable.

The plumes developing at the injection point were monitored over time as they progressed downgradient. In both lanes there was an initial advance of the plumes. Both plumes then retracted but the With-Ethanol Lane plume retracted more slowly. Rates of benzene degradation increased with time. In the With-Ethanol Lane, sulfate was depleted and methane was produced, and BT*o*X degradation occurred both in the core of the plume and also along the plume fringes by sulfate reduction. Finally, the methane-rich and sulfate-depleted zones along the With-Ethanol Lane were restricted in space.

Feris et al. [2008] described the observed effect of ethanol on the microbial community structure and natural attenuation during the same experiments. In both lanes there was an increase in SRB and total bacteria. The total bacteria increase extended farther in the With-Ethanol Lane (9.4 m; EC transect) than in the No-Ethanol Lane (5.5 m; EB transect). Only the With-Ethanol Lane had an increase in archaea. In the No-Ethanol Lane the injected concentration of reduced carbon was too low to significantly affect redox conditions except very near the injection wells. In contrast, in the With-Ethanol Lane the reduced carbon stimulated SRB growth resulting in complete consumption of sulfate. Archaea in the With-Ethanol Lane reached a maximum density 5.5 m downgradient (EB transect) after 152 days

and at the injection wells (ER transect) after 244 days. In this lane ratios of SRB to total bacteria decreased dramatically over the course of the experiment [*Feris et al*., 2008].

3. Model description

3.1. Conceptual model

The biodegradation kinetics adopted in this model link ethanol degradation, microbial growth, and BT*o*X biodegradation under different redox conditions. Previous monitoring data from the site show that neither oxygen nor nitrate is a significant electron acceptor in the study aquifer [*Rasa*, 2012]. Therefore, the model includes only iron-reducing and sulfate-reducing degradation of BT*o*X, ethanol, and methane and fermentative-methanogenic degradation of ethanol. The model describes the distribution over time and space of 14 species, with seven aqueous or mobile chemical compounds (benzene, toluene, o-xylene, ethanol, acetate, sulfate, and methane), the immobile solid phase iron oxyhydroxide, and six immobile microbial populations. The six microbial populations are: BT*o*X-degrading iron-reducing bacteria, BT*o*X-degrading SRB, ethanol-degrading iron-reducing bacteria, ethanol-degrading SRB, ethanol-degrading fermentative bacteria, and acetate-degrading methanogenic archaea. The only mass transfer mechanism between the immobile and aqueous phases in the model is sorption. The bacteria grow in place and affect reaction rates. The immobile iron oxy-hydroxides are depleted by iron reduction.

The conceptual model for the flow system has been discussed elsewhere [*Mackay et al*., 2012; *Mackay et al*., 2006] and used in other simulations [*Rasa et al*., 2011]. The model domain in this work is quasi-three dimensional with three horizontal layers: an upper silty aquitard (0.6 m thick), a thin sandy aquifer (0.8 m thick), and a lower silty aquitard (0.9 m thick), as shown in cross-section in Fig. 2. The model domain is 110 m along the direction of groundwater flow (*x*), 55 m in the direction perpendicular to the groundwater flow (*y*), and 2.3 m in the vertical direction (*z*). The simulation time was 283 days. Groundwater flow was assumed to be steady state with no sinks and a constant hydraulic gradient of 0.0132. Transport parameters and concentrations used in the model are given in Table 1. Hydrogeological properties including porosity and hydraulic conductivity of the aquifer and aquitard layers are based on site-specific analyses or literature.

Injection wells (labeled ER; Fig. 2) were simulated by adding spiked background groundwater at 3.3×10^{-3} L/s. The initial and upstream boundary concentrations of sulfate were set to the background concentration of 120 mg/L. The initial concentration of poorly crystalline iron oxy-hydroxide was assumed uniform in the experimental area and set to 1,000 mg/kg as Fe [*Wood*, 2004]. The injection concentrations of BT*o*X and ethanol compounds and initial concentrations of other compounds are also listed in Table 1. Water samples taken from between the two experimental plumes and also upgradient of the injection source were used to provide an estimate of the pre-experimental background microbial populations. *Feris et al*. [2008] reported average values of 2.8×10^{4} of bacterial 16S gene copies/mL, 1.7×10^{2} copies of SRB, and 1.4×10^{3} archaeal 16S copies/mL for the regions of the aquifer unaffected by the controlled releases.

3.2. Governing equations

In this study the groundwater flow system is assumed at steady state with constant head boundary conditions, a uniform groundwater flow gradient, and groundwater injection wells. The three-dimensional advection-dispersion equation of a reactive compound is described in Eq. (1). Equation (2) describes the reaction of an immobile compound:

$$Rf_i\,\theta^k\frac{\partial C_i}{\partial t}=\theta^k D_x\frac{\partial^2 C_i}{\partial x^2}+\theta^k D_y\frac{\partial^2 C_i}{\partial y^2}+\theta^k\,D_z\frac{\partial^2 C_i}{\partial z^2}-\theta^k\upsilon_x\frac{\partial C_i}{\partial x}-\theta^k\upsilon_y\frac{\partial C_i}{\partial y}-\theta^k\upsilon_z\frac{\partial C_i}{\partial z}+q^s\,C_i^s+R_i\quad i=1,7 \quad (1)$$

$$\frac{\partial C_{im}}{\partial t}=R_{im}\quad im=1,7 \quad (2)$$

where, Rf_i is the retardation factor of compound *i*, θ^k is the porosity of the media *k* [-], υ is groundwater velocity [LT^{-1}], C_i is the aqueous-phase (mobile) concentration of compound *i* [ML^{-3}], C_{im} is the solid-phase (immobile) concentration of compound *im*, q^s is volumetric flow rate per unit volume of aquifer representing fluid sources and sinks [T^{-1}], C_i^s concentration of the source or sink flux for component *i* [ML^{-3}], R_i R_{in} and R_{im} are the net reaction rates of i_{th} compounds *i* and *im* respectively [$ML^{-3}T^{-1}$]. The source well injection rate is q^s and source concentration of solute i is C_i^s. The seven mobile and immobile compounds are specific to this study and they are defined in section 3.1. D_x, D_y, and D_z are the longitudinal, horizontal and vertical hydrodynamic dispersion coefficients [L^2T^{-1}], respectively, where $D_x = \alpha_L\,\upsilon + \tau D_m$, $D_y = \alpha_T\,\upsilon + \tau D_m$, and $D_z = \alpha_V\,\upsilon + \tau D_m$. α_L, α_T, and α_V are the longitudinal, horizontal and vertical dispersivities [L], respectively, D_m is the aqueous molecular diffusion coefficient [L^2T^{-1}], and τ is tortuosity [-] [*Scheidegger*, 1961].

3.3. Reaction kinetics

Multiple Monod terms [*Molz et al*., 1986; *Monod*, 1949] were used to account for the effect of different electron acceptors on degradation rates under each pathway. Eqs 5-27 show rate equations that account for the anaerobic and methanogenic biodegradation of ethanol and BT*o*X and associated biomass growth. Due to the low biomass yield in this study (1-5%) compared to substrate utilization, we did not include the carbon incorporated into biomass in the reaction stoichiometry. Inhibition terms are added to these rate equations to account for the succession of redox conditions. Table 2 presents the definition and assigned or calibrated values of all the parameters used in the kinetics equations. For conciseness, the definitions of the variables are not repeated in the text.

Degradation of benzene, toluene, and *o*-xylene—Benzene can degrade under iron reduction, sulfate reduction, and methanogenesis [*NRC*, 2000]. However, in this work, we did not consider methanogenic reactions of benzene, because this reaction is considered unreliable [*NRC*, 2000]. Eqs. 3 and 4 describe benzene degradation under iron-reducing and sulfate-reducing conditions, respectively.

$$C_6H_6+30Fe(OH)_3+60H^+\rightarrow 30Fe^{2+}+6CO_2+78H_2O \quad (3)$$

$$4C_6H_6+15SO_4^{2-}+12H_2O\rightarrow 24HCO_3^-+15HS^-+9H^+ \quad (4)$$

Mass ratios used for toluene and *o*-xylene degradation under iron reduction and sulfate reduction are given in Table 2 and the reactions are given in *Rasa* [2012].

Under iron-reducing conditions the individual reaction rates of BT*o*X are:

$$R_{Fe}^B=-R_{max_{Fe}}{}^B\left(\frac{B}{K_B+B}\right)\left(\frac{Fe}{K_{Fe}+Fe}\right)f_{EtOH} \quad (5)$$

Eq. 5 reflects an assumption that growth of iron-reducing bacteria on BT*o*X is negligible (see Biomass Growth section). The flag f_{EtOH} inhibits BT*o*X degradation in the presence of ethanol. A microcosm study of ethanol fermentation by *Adair and Wilson* [2012] showed that if ethanol is present above 1 mg/L, the concentration of its degradation products will be high enough to inhibit the biodegradation of benzene. The adoption of the same ethanol threshold for iron-reducing and sulfate-reducing conditions is based on the assumption that complex molecules are converted to acetate, followed by acetate oxidation coupled to a favorable electron acceptor. Thus, build-up of acetate can theoretically inhibit the transformation of ethanol to acetate regardless of the electron acceptor. Therefore, we have assumed f_{EtOH} equals 0 when the ethanol concentration is above 1 mg/L. When the ethanol concentration is below 1 mg/L, the value of this factor is 1. R^T_{Fe} and R^X_{Fe} rates are computed similarly to R^B_{Fe}.

Eq. 6 presents the reaction rates of BT*o*X compounds under sulfate reduction. We did not include any inhibition of sulfate reduction in the presence of ferric iron, as simultaneous degradation under iron-reducing and sulfate-reducing conditions has been observed in several field studies (e.g., *Postma and Jakobsen*, 1996). The reaction rate depends on the population of BToX-degrading SRB, S_2, which changes with time:

$$R^B_{SO_4} = -\frac{\mu^B_{S_2} S_2}{Y^B_{S_2}} \left(\frac{B}{K_B + B}\right) \left(\frac{SO_4}{K_{SO_4} + SO_4}\right) f_{SO_4} f_{EtOH} \quad (6)$$

where f_{SO_4} is a flag for limiting sulfate reduction when sulfate concentration is below a threshold. Our field data suggest that sulfate reduction was limited where sulfate concentration was below 15 mg/L since an average sulfate concentration of about 15 mg/L remained along the centerline of the plume. The value of f_{SO_4} is 1 when sulfate concentration is higher than 15 mg/L. Otherwise f_{SO_4} is 0 making sulfate unavailable for additional reduction (Table 2). $R^T_{SO_4}$ and $R^X_{SO_4}$ rates are computed similarly to $R^B_{SO_4}$.

The overall BT*o*X utilization rate is obtained by adding the rates for degradation under iron-reducing and sulfate-reducing conditions:

$$R^B = R^B_{Fe} + R^B_{SO_4} \quad (7)$$

As before, R^X and R^T rates are computed similarly to R^B.

Degradation of ethanol—Anaerobic degradation of ethanol under iron-reducing and sulfate-reducing conditions occurs with the following stoichiometric relations [*Chen et al*., 2008]:

$$CH_3CH_2OH + 12Fe(OH)_3 + 24H^+ \rightarrow 12Fe^{2+} + 2CO_2 + 33H_2O \quad (8)$$

$$2CH_3CH_2OH + 3SO_4^{2-} + 6H^+ \rightarrow 3H_2S + 4CO_2 + 6H_2O \quad (9)$$

In the absence of external electron acceptors, ethanol can degrade to acetate and molecular hydrogen [*Dolfing*, 2001]. The generated acetate is fermented to carbon dioxide and methane under acetoclastic methanogenesis:

$$CH_3CH_2OH + H_2O \rightarrow CH_3COO^- + H^+ + 2H_2 \quad (10)$$

$$CH_3COO^- + H^+ \rightarrow CH_4 + CO_2 \quad (11)$$

The ethanol degradation rates under iron reduction (Eq. 12), sulfate reduction (Eq. 13) and fermentation to acetate (Eq. 14) are presented below:

$$R_{Fe}^{EtOH} = -\frac{\mu_{S_3} S_3}{Y_{S_3}^{EtOH}} \left(\frac{EtOH}{K_{EtOH} + EtOH}\right) \left(\frac{Fe}{K_{Fe} + Fe}\right) \quad (12)$$

$$R_{SO_4}^{EtOH} = -\frac{\mu_{S_4} S_4}{Y_{S_4}^{EtOH}} \left(\frac{EtOH}{K_{EtOH} + EtOH}\right) \left(\frac{SO_4}{K_{SO_4} + SO_4}\right) f_{SO_4} \quad (13)$$

$$R_{CO_2}^{EtOH} = -\frac{\mu_{S_5} S_5}{Y_{S_5}^{EtOH}} \left(\frac{EtOH}{K_{EtOH} + EtOH}\right) \left(\frac{K_{SO_4}^i}{K_{SO_4}^i + SO_4}\right)^2 \left(\frac{K_{Fe}^i}{K_{Fe}^i + Fe}\right)^2 \quad (14)$$

In Eq. 14, we utilize a modified form of the inhibition function (the last term). We performed numerical tests (not shown here) which suggested a better match of simulations to observed data was obtained when $\left(\frac{K_{SO_4}^i}{K_{SO_4}^i + SO_4}\right)^2$ was used as an inhibition function instead of the more commonly utilized $\frac{K_{SO_4}^i}{K_{SO_4}^i + SO_4}$ [*Rasa*, 2012]. The proposed second-order function strongly inhibited methanogenesis in the presence of 40 mg/L (or more) of sulfate and below 40 mg/L it quickly approached 1, allowing maximum methanogenic rates to be applied.

The overall ethanol utilization rate is obtained by adding the rates from the three degradation pathways assumed here (iron reduction, sulfate reduction, and methanogenesis):

$$R^{EtOH} = R_{Fe}^{EtOH} + R_{SO_4}^{EtOH} + R_{CO_2}^{EtOH} \quad (15)$$

One of the intermediate products of ethanol degradation under methanogenic conditions is acetate (Eq. 10). Acetate is then fermented to methane (Eq. 11). The overall reaction rate of acetate is:

$$R^{Acet} = -Y_{Acet}^{EtOH} R_{CO_2}^{EtOH} + R_{CH_4}^{Acet} \quad (16)$$

where $R_{CH_4}^{Acet} = -\frac{\mu_{S_6} S_6}{Y_{S_6}^{Acet}} \left(\frac{Acet}{K_{Acet} + Acet}\right)$ is the transformation rate of acetate to methane.

Methane generation and anaerobic oxidation—Biodegradation of methane coupled to both sulfate [*Martens and Berner*, 1977] and iron [*Beal et al*., 2009] was included in this

modeling study. Methane oxidation coupled with sulfate reduction is described by [*Martens and Berner*, 1977]:

$$CH_4+SO_4^{2-}+2H^+ \rightarrow CO_2+H_2S+2H_2O \quad (17)$$

The equation for methane oxidation coupled with iron reduction [*Beal et al*., 2009] is:

$$CH_4+8Fe\,(OH)_3+15H^+ \rightarrow HCO_3^-+8Fe^{2+}+21H_2O \quad (18)$$

The rate of change in dissolved methane concentration is then:

$$R^{CH_4}=-Y_{CH_4}^{Acet}R_{CH_4}^{Acet}+f_{SO_4}R_{SO_4}^{CH_4}+R_{Fe}^{CH_4} \quad (19)$$

where $R_{SO_4}^{CH_4}$ and $R_{Fe}^{CH_4}$ are the zero-order rates of anaerobic methane oxidation under sulfate-reducing and iron-reducing conditions, respectively. We assume zero order rates for reasons discussed later.

Depletion rate of electron acceptors—Iron reduction (Eq. 20) and sulfate reduction rates (Eq. 21) are calculated using the substrate utilization rates and the reaction mass ratios in Table 2:

$$R^{Fe}=Y_{Fe}^{B}R_{Fe}^{B}+Y_{Fe}^{T}R_{Fe}^{T}+Y_{Fe}^{X}R_{Fe}^{X}+Y_{Fe}^{EtOH}R_{Fe}^{EtOH}+Y_{Fe}^{CH_4}R_{Fe}^{CH_4} \quad (20)$$

$$R^{SO_4}=Y_{SO_4}^{B}R_{SO_4}^{B}+Y_{SO_4}^{T}R_{SO_4}^{T}+Y_{SO_4}^{X}R_{SO_4}^{X}+Y_{SO_4}^{EtOH}R_{SO_4}^{EtOH}+Y_{SO_4}^{CH_4}R_{SO_4}^{CH_4} \quad (21)$$

Biomass growth—The growth rates of different populations are calculated based on the substrate utilization rates and the biomass yield. Because of the low Gibbs free energy values reported for anaerobic oxidation of methane [*Regnier et al*., 2011], we assumed no biomass growth due to methane degradation. Other studies such as *Bekins et al*. [1993] have reported biodegradation with no apparent growth under methanogenic conditions. We also assumed no growth of iron-reducing bacteria due to BT*o*X degradation in the presence of ethanol (Eq. 22). This assumption is consistent with the linear profile of benzene loss in the With-Ethanol Lane observed in the experiment, which indicates a constant microbial population (e.g. *Bekins et al*., 1993). Eqs. 22 to 27 relate the growth of the six microbial populations to the biodegradation of BToX under iron-reducing (Eq. 22) and sulfate-reducing conditions (Eq. 23), ethanol under iron-reducing (Eq. 24), sulfate-reducing (Eq. 25), and methanogenic conditions (Eq. 26), and acetate under methanogenic conditions (Eq. 27):

$$R^{S_1}=0 \quad (22)$$

$$R^{S_2}=-(Y_{S_2}^{B}R_{SO_4}^{B}+Y_{S_2}^{T}R_{SO_4}^{T}+Y_{S_2}^{X}R_{SO_4}^{X})-b_1S_2 \quad (23)$$

$$R^{S_3}=-Y_{S_3}^{EtOH}R_{Fe}^{EtOH}-b_1S_3 \quad (24)$$

$$R^{S_4} = -Y_{S_4}^{EtOH} R_{SO_4}^{EtOH} - b_1 S_4 \quad (25)$$

$$R^{S_5} = -Y_{S_5}^{EtOH} R_{CO_2}^{EtOH} - b_1 S_5 \quad (26)$$

$$R^{S_6} = -Y_{S_6}^{Acet} R_{CH_4}^{Acet} - b_2 S_6 \quad (27)$$

where b_1 and b_2 are the decay rates of bacteria and archaea, respectively (Table 2). Total iron-reducing bacteria (IRB) and total SRB are given by $S_1 + S_3$ and $S_2 + S_4$, respectively. The concentration of total bacteria (which includes IRB, SRB, and fermentative bacteria) is calculated as the sum of all bacteria populations ($S_1 + S_2 + S_3 + S_4 + S_5$). The concentration of total archaea is S_6.

3.4. Conversion between gene copy numbers and biomass concentration

A common unit used for reactive transport models is mass per aqueous-phase volume. Here the modeled biomass (S_1 through S_6) was in units of mg of dry weight of cells per liter of aqueous-phase volume. Experimental data are in units of gene copy numbers per mL of water determined by qPCR [*Feris et al*., 2008]. *Rittmann and McCarty* [2001] suggest there are about 10^{12} bacteria in a gram of biomass (dry solid weight). We assumed the same dry solid density for archaea.

The number of rRNA genes can vary from 1-15 copies per prokaryote cell [*Klappenbach et al*., 2001]. Although the range observed in gene copy number is quite large, there is some relationship to phylogenetic grouping. According to the database developed by *Klappenbach et al*. [2001], the ratio of gene copies per cell averages 5 for bacteria and 1.7 for archaea.

In this modeling study, biomass is considered attached (i.e., immobile). However, field data were from water samples and therefore represent planktonic (suspended) cells. *Bekins et al*. [1999] compared suspended versus attached populations of 76 sample pairs from an aquifer contaminated by crude oil and suggested that an average of 15% of the total population is suspended. The relative population density of planktonic bacteria to total bacteria also was measured by *Harvey and Barber* [1992], who reported a planktonic to total bacteria ratio of 7- 31% in a sewage-contaminated groundwater. Here, we assume 15% of total population is planktonic. Thus, to compare microbial qPCR data (copies/mL) with the simulated biomass, we multiplied simulated biomass concentrations (mg/L) by (10^{12} cells/g)×(10^{-3} g/mg)×(10^{-3} L/mL)×15/85×(gene copies per cell). Our conceptual model is that growth takes place in the attached phase and that this is reflected as a proportionate increase in the adjacent planktonic numbers. Therefore, planktonic bacteria were assumed to follow the same distribution as the attached population at the sampling locations and transport of cells was not included in the model.

3.5. Numerical solution

We used the U.S. Geological Survey MODFLOW model [*Harbaugh et al*., 2000] to solve for groundwater flow. Grid discretizations of 0.2 m and 0.2 m were used in the *x* and *y* directions, respectively. The simulation time was 283 days, with average transport time steps of 0.02 days. A head change value of 0.01 cm was used as the convergence criterion. The reactive transport system (Eqs. 1-2) was implemented and numerically solved using RT3D v2.5 [*Clement et al*., 1998]. The standard finite difference solver (upstream weighting) was used to solve the advection term, while the standard explicit method was used to solve the dispersion term. To solve the reaction terms, the Gear solver with explicit Jacobian was

applied. Peclet and Courant criteria were checked (not discussed here) to ensure convergence and stability of the transport model. Absolute and relative tolerance parameter values of 10^{-13} and 10^{-12} were used, respectively, to control the convergence of the reactive transport of all components in the model.

4. Results and discussion

The simulated steady-state flow field used for the transport model is shown in Fig. SI.1. The flow system diverged slightly outward in the vicinity of the injection wells but had parallel flow paths downgradient of the injection wells.

4.1. Ethanol and BT*o*X

Figs. 3 through 11 compare the simulated versus measured concentrations of different compounds along the plume centerlines. For the measured data, the centerline is defined to include the monitoring well in each transect with highest substrate concentration at any given time in the With-Ethanol and No-Ethanol Lanes. For the simulated results, the centerline is the center row in the model grid.

During the experiment simulated here, ethanol was detected in groundwater only rarely and only at one location at 0.5 m downgradient of the injection wells in With-Ethanol Lane [*Feris et al*., 2008; *Mackay et al*., 2006]. Because there are so few ethanol data from the field experiment, we do not present plots comparing measured and simulated ethanol over time. Although the ethanol data were limited, the ethanol degradation rate parameters were constrained by the loss of electron acceptors and the production of methane.

Figs. 3a and 3c present the measured benzene concentrations in the With-Ethanol and No-Ethanol Lanes, respectively. Several important features of the data needed to be captured by the model. First, benzene degraded in portions of both lanes under sulfate-reducing conditions. Therefore we coupled benzene degradation to sulfate reduction in the model (Eq. 6). The second feature of the benzene data was that the benzene degradation rate increased with time in the No-Ethanol Lane and after 274 days the benzene plume was limited to the first 3 m downgradient of the source (Fig. 3c). This suggests that growth of benzene-degrading, SRBs (S_2) is important (Eq. 23). The third aspect was the 4.5 times greater length of the benzene plume in the With-Ethanol Lane. In the model the inhibition of benzene degradation in the presence of 1 mg/L of ethanol (f_{EtOH}) was required to simulate initial advance of the benzene plume. The benzene degradation begins after the ethanol-degrading population has grown sufficiently large to degrade ethanol upgradient of the first sample transect. A fourth feature of the data is that in the With-Ethanol Lane, benzene degraded even after ethanol degradation depleted most of the available sulfate, suggesting benzene degradation coupled to iron reduction was also required in the model (Eq. 5). However, benzene degradation rates did not change significantly over time in the With-Ethanol Lane (Fig. 3a), suggesting that benzene-degrading, iron-reducing bacteria (S_1) were not growing over time (Eq. 22). Comparing the model results in Figs. 3b and 3d with the data in Figs. 3a and 3c shows that including SRB growth, ethanol inhibition, and degradation by iron reduction captured the differing benzene behavior in the No-Ethanol and With-Ethanol Lanes.

The fate of toluene differed somewhat from that of benzene (Figs. 4a and 4c). There was a similar initial advance of the plume and retraction in the With-Ethanol Lane due to inhibition of degradation by ethanol. Also degradation of toluene in the With-Ethanol Lane was slower compared to the No-Ethanol Lane because of the depletion of sulfate after 64 days. So toluene degradation is coupled to iron reduction downgradient of 3 m. Unlike benzene, toluene concentrations dropped below the detection limit throughout the

experimental area (with just a few exceptions, all near the detection limit) by the end of the experiment in the With-Ethanol Lane. This feature was captured by the model through a higher growth rate of toluene-degrading SRB relative to benzene-degrading SRB ($\mu^{T}_{S_2}$, Table 2). As a result, once ethanol is below 1 mg/L upgradient of 3 m, degradation of toluene proceeds faster than benzene degradation consuming available sulfate near the injection well. As presented in Fig. 4b and 4d, simulation results showed very good agreement with the toluene data from both lanes.

Data from the field experiment showed *o*-xylene behaved similarly to benzene, persisting within 13 meters downgradient of the ethanol injection source after 274 days (Figs. 5a and 5c). Therefore the same approach used for benzene degradation was used for *o*-xylene. Comparison of simulated versus measured data (Fig. 5) shows that the model could explain the important features of *o*-xylene data over time and space.

4.2. Sulfate, Iron and Methane

Figs. 6a and 6c present measured sulfate data at 170 days. One important feature of the sulfate data was that sulfate was reduced to 10-15 mg/L within the methanogenic zone in the With-Ethanol Lane and then remained constant (Fig. 6a). This does not appear to be due to substrate limitation because within 13 meters of the injection source in the With-Ethanol Lane, there are still relatively high concentrations of methane (10 to 29 mg/L), benzene (0.5 to 2 mg/L) and *o*-xylene (0.1 to 0.6 mg/L) within the aquifer. To capture this feature, we used a flag (f_{SO_4}) to limit the availability of dissolved sulfate for all sulfate reduction pathways below the threshold of 15 mg/L that was observed in the field data (Eqs. 6, 13, and 19).

A second important feature of the sulfate data was the increase in sulfate concentration beyond 35 meters downgradient from the source (Fig. 6a). Simulations suggested that this is due to vertical mixing of sulfate-depleted groundwater in the aquifer with sulfate-rich groundwater entering from the upper and lower silty aquitard layers through vertical dispersion and diffusion. Earlier versions of the model used in this study only included the aquifer layer and not the adjacent aquitards. Comparing the results of the same reactive transport model with and without the aquitard layers (results not presented here) suggested that the aquitard layers provided the additional sulfate to the aquifer downgradient of the source.

Simulated sulfate concentrations in Figs. 6b and 6d indicate that the model with aquitard layers and the sulfate threshold could reproduce the behavior of the sulfate plume in the presence and absence of ethanol. Threshold limitations in sulfate reduction have been reported by other studies [*Knab et al*., 2008; *Roychoudhury and McCormick*, 2006; *Roychoudhury et al*., 2003]. Possible explanations for the limitation of sulfate reducers may be the presence of toxic concentrations of sulfide or competition from other microbial populations with respect to mineralizable organic carbon, as reported by *Roychoudhury and McCormick* [2006]. *Leloup et al*. [2007] suggested there may be a threshold concentration below which sulfate is not bioavailable to SRB. Finally, *Knab et al*. [2008] reported at concentrations below 0.2 mM (19.2 mg/L) sulfate was not readily available for anaerobic oxidation of methane in marine sediments. This study may be the most relevant to the VAFB plume because the main reduced carbon source beyond 13 m downgradient was methane.

Upgradient of 13 m BToX is still present and could be coupled to sulfate reduction. Other studies of BTEX degradation coupled to sulfate reduction have presented data indicating that sulfate concentrations may remain above 10 mg/L when benzene is present at greater

than 1 mg/L. *Anderson and Lovley* [2000] studied the transient effect of sulfate addition to a benzene contaminated aquifer and found that sulfate initially decreased and then remained level at 100-200 μmol/l (10-19 mg/l) with benzene at 20-30 μmol/l (1.5-2.5 mg/l). A study of a BTEX plume by *Davis et al*. [1999] indicated that the mean sulfate concentration was 10.8 mg/l in areas of the plume where benzene was greater than 1 mg/l. These results are consistent with the observation that sulfate remains at 15 mg/L at VAFB even when BT*o*X and methane were present.

Measurements of ferric iron concentration were available only prior to the field experiment; therefore no comparison could be made to iron values simulated during the experiment (Fig. 7). Simulations suggested that a greater amount of ferric iron was reduced in the With-Ethanol Lane. This is due to the inclusion in the model of anaerobic degradation of methane coupled to iron reduction. The importance of this process in the simulations is discussed further below.

Fig. 8a shows the measured concentration of dissolved methane along the plume centerline in the With-Ethanol Lane. Three important features of the data needed to be captured by the model. First, methane concentrations measured at 64 days were within the levels observed at the site prior to this experiment, indicating an increase in rate and spatial extent of methanogenesis occurred after this time. To reproduce this feature of the data, methanogenesis was inhibited in the presence of sulfate according to Eq. 14 and ethanol was first fermented to acetate before being transformed to methane. These two changes to the model delayed methanogenesis until after 64 days, but the simulated methane concentrations at 115 days are higher than the observed values suggesting that an additional unknown process delayed the start of methane production in the field experiment. Possible candidates not included in the model are toxicity of ethanol, fluctuations in injected sulfate concentration, or greater accumulation of acetate.

The second important feature is that after 115 days there is a linear decrease in methane concentration with distance from the injection source, indicating a loss mechanism for methane. To capture this loss the model includes anaerobic oxidation of methane coupled to both sulfate and iron reduction. Recent studies have indicated that methane oxidation may be coupled to iron reduction [*Beal et al*., 2009; *NRC*, 2000]. The inclusion of iron was required by the continued loss of methane in a zone where sulfate was below the posited thermodynamic threshold of 15 mg/L. Results suggested a degradation rate of 0.28 mg/L/day for anaerobic oxidation of methane coupled to iron (Table 2). The maximum degradation rate for anaerobic oxidation of methane coupled to sulfate $(R_{SO_4}^{CH_4})$ was 0.04 mg/L/day. Modeling results indicated that by the end of 283 days, sulfate reduction could account for 12% (1.6 kg) of the methane degradation while 88% (13 kg) of methane degradation was through iron reduction. The third important feature of the methane data is that after 200 days the highest concentration of dissolved methane in water samples remained constant at 29 mg/L which is within the range of methane solubility in groundwater [*Lee et al*., 2009]. These data indicate that methane produced near the source after 200 days was degassing. Thus, in the simulations we assumed that any methane concentration above the 29 mg/L threshold could degas from the system. This was implemented using a maximum concentration for the dissolved methane (29 mg/L), replacing the methane values above this threshold assuming the excess methane left the dissolved phase. Fig 8b compares the corresponding simulated values of methane concentration. The correspondence of simulated and observed methane values when both degassing and anaerobic methane oxidation by sulfate and iron reduction were included indicates the importance of these processes at ethanol and hydrocarbon contaminated sites.

Degassing of methane from groundwater aquifers has been previously reported and investigated in several studies. *Amos et al*. [2005] studied the production and transport of methane at Bemidji crude oil spill site and using inert gasses provided evidence that a considerable amount of methane was lost due to degassing. Results of a more recent study by *Ma et al*. [2012] showed that methane concentrations in an aquifer exposed to a continuous release of a 10% ethanol solution (by volume) reached the saturation level in groundwater and methane was detected in a surface flux chamber indicating that degassing was an important process. *Spalding et al*. [2011] also suggested that methane can migrate from the subsurface at ethanol spill sites and present vapor risks for nearby confined spaces with ignitable conditions. Generation of explosive levels of methane were reported by *Nelson et al*. [2010] where a continuous feed of dilute E85 was used for a column study.

Caldwell et al. [2008] showed that anaerobic oxidation of methane coupled to iron is energetically favorable. The study by *Beal et al*. [2009] showed that anaerobic oxidation of methane may be coupled to reduction of manganese and iron. In a methanogenic crude oil contaminated aquifer near Bemidji, Minnesota, methane isotope analyses by *Amos et al*. [2012] indicated microbial oxidation of methane in an anaerobic portion of the plume. They argued that iron-mediated anaerobic oxidation of methane was occurring based on the dominance of the Fe(III)-reducing genus *Geobacter* and mass balance calculations of reduced carbon flux and depletion of labile sediment iron. *Crowe et al*. [2011] presented evidence of methane oxidation at Lake Matano and argued that the oxidation was coupled to iron reduction based on the abundance of ferric iron and absence of oxygen, sulfate, and nitrate. Numerical modeling presented in this study, along with field observations, suggest that methane degradation occurred in an area of the plume where iron was the only available electron acceptor. Although the species involved and the reaction pathway for anaerobic oxidation of methane coupled to iron reduction are still unknown, the mass balance in the modeling and observed constant degradation rate in the field are consistent with this process. Figs. 9a and 9b present the simulated cumulative amounts of methane oxidation through iron reduction and sulfate reduction pathways, respectively, indicating a zone within the plume where methane degradation coupled to sulfate reduction was limited and iron reduction was the only available process for methane oxidation. The total amount of methane oxidation coupled to iron reduction was about eight times more than by sulfate reduction (13 kg and 1.6 kg respectively). This finding is consistent with our field observations suggesting that methane oxidation was occurring along the plume centerline (Fig. 8a).

The aquitard layers were added to the model to investigate whether the observed loss of methane could be caused by either diffusion into the aquitards or by reaction with sulfate diffusing from the aquitards. The numerical dispersion associated with the low vertical resolution in the quasi-3D model represents a maximum amount of exchange with the aquitard, yet this is still inadequate to explain the methane loss. The results support the suggestion that the observed methane loss may be coupled to iron reduction. Numerical dispersion of BT*o*X into the aquitard layers did not change the calibrated reaction rates. Our modeling results before and after addition of the aquitard layers indicated no changes were required to the kinetic parameters.

4.3. Bacteria and Archaea

Field data suggest that densities of total bacteria, SRB, and archaea populations were up to four orders of magnitude higher within the experimental lanes relative to the background levels [*Feris et al*., 2008]. Simulation of transient growth of biomass at a field site is challenging. First, because the data are sparse in time and space and comparison of model results to data requires assumptions about the relationship between attached and planktonic biomass and conversion between qPCR data and cell density. Second, accumulation of

biomass has a positive feedback because it leads to faster degradation rates which in turn lead to faster growth, so it is difficult to achieve orders of magnitude increases in biomass in a simulation without exceeding the observations. Recognizing these challenges, we iterated during our simulation efforts to generate the most reasonable estimates of growth and rates given the field observations and results of prior studies.

Growth rates of bacteria and archaea in the model are controlled by the parameters listed in Table 2 together with the substrate and electron acceptor concentrations (e.g. Eq. 6). Growth yields were calibrated for ethanol degradation by SRB and fermenters and acetate degradation by methanogens. The remaining yields were based on energetic calculations as described in *Rittmann and McCarty* [2001]. Figs. 10 through 12 present the comparison between biomass data and numerical simulations. Field data are presented as the average of three values from sampling wells in the center of the experimental lanes with bars representing maximum and minimum values. Simulated values are converted to copy numbers per mL of groundwater for comparison with the data.

At 244 days the model reproduces the observed increase of SRB of two to four orders of magnitude in both lanes relative to the background level (Fig. 10). The greatest increase occurs adjacent to the injection wells because the injected groundwater in both lanes contained background concentrations of sulfate. The model SRB values were 10^6 per mL near the injection well in both lanes at 244 days whereas field results were 10^5 per mL indicating that the model overpredicted growth near the injection wells. Downgradient of the injection wells, the model results were 10^4-10^5 per mL SRB in the With-Ethanol Lane at 244 days compared to averages of 10^3-10^5 per mL in the field. In the No-Ethanol Lane the model results were 10^3-10^4 per mL SRB compared to field values of 10^2-10^4 per mL in the field. Thus, at the most downgradient locations the simulated SRB values were about ten times too high in the With-Ethanol Lane but matched well in the No-Ethanol Lane. In the With-Ethanol Lane, the abundance of SRB decreased slightly between 152 and 244 days at the injection well [*Feris et al*., 2008]. The simulations also show a decrease in SRB between 152 and 244 days but located downgradient of the injection wells (Fig. 10b). The simulated SRB decrease occurs in the With-Ethanol Lane because the sulfate concentration was below the posited thermodynamic threshold of 15 mg/L (Fig. 6a). The high concentration of injected ethanol and growth of SRB resulted in consumption of available sulfate below the threshold of 15 mg/L, which was followed by a decline of the SRB at later times. In the No-Ethanol Lane populations initially expanded as the BT*o*X plume advanced downgradient. The higher populations lead to faster BT*o*X degradation rates and shrinking of the BT*o*X plume. Even though sulfate was high, the SRB population declined due to the lower BT*o*X concentrations.

The simulations reproduced the trend of the total bacterial density data (which include iron-reducing, sulfate-reducing, and fermentative bacteria) in that the highest concentration for both With-Ethanol and No-Ethanol Lanes occurred adjacent to the injection wells (Fig. 11), similar to what was reported by *Feris et al*. [2008]. Simulations produced 1.5-2 orders of magnitude more growth in the With-Ethanol than the No-Ethanol Lane due to the greater supply of reduced carbon with the ethanol injection. Simulations suggest that growth of total bacteria populations in the No-Ethanol Lane was due to the growth of SRB. In the With-Ethanol Lane, however, the model suggested that growth of fermentative bacteria contributed the most to the increase in the densities of total bacteria. *Feris et al*. [2008] indicated that elevated values in the With-Ethanol Lane extended beyond 7 m downgradient, whereas the elevated values in the No-Ethanol Lane were limited to the first 3 m (Figs 11a and 11c). The model reproduces the elevated values at 7 m in the With-Ethanol Lane but also predicts some growth downgradient (Fig 11b).

In the No-Ethanol Lane the model predicts growth near the injection wells and values similar to background levels downgradient of 3 m (Fig. 11d), which is consistent with the trend of the field data. However, the model cannot explain the very high value of 10^8 per mL total bacteria observed at 244 days near the injection well in the No-Ethanol Lane and the comparatively lower bacterial densities in the With-Ethanol Lane. Possibly this reversal was due to lower energetic yield of fermentation of ethanol to acetate followed by methanogenesis from acetate, processes which dominate at late time in the With-Ethanol Lane. Consistent with this explanation, the data earlier in the experiment (152 days Figs 10 and 11) show SRB and total bacterial densities were higher in the With-Ethanol Lane that in the No-Ethanol Lane. In this earlier period the biomass level in the With-Ethanol Lane may still have reflected some contribution of the sulfate-reducing metabolism and higher yield, e.g. if sulfate was supplied to the permeable media by diffusion from lower permeability layers before their reservoirs of sulfate were exhausted. Nevertheless, when the model yields were calibrated to the full data set, the same values were obtained for SRB and fermenting bacteria (Table 2), suggesting further investigation into the yields in such dynamic settings could prove illuminating.

A notable discrepancy between the model and data occurs at the most downgradient point, where the No-Ethanol Lane data show almost 10^6 per mL bacteria versus fewer than 10^5 per mL in the model. These differences may occur because the model simulates attached populations while the observations represent suspended cells. If 15% of the population growing near the injection wells had been transported downgradient, then the observed numbers in the No-Ethanol Lane could have resulted from transport of these cells. We based our conversion of attached to planktonic numbers on the data of Bekins et al. [1999] for the Bemidji site. Their data showed similar ratios throughout the plume with no indication that transport of the planktonic phase increased numbers in the downgradient region of the plume. Whether the planktonic cells were transported downgradient at the VAFB site is unknown, but some evidence of transport is suggested by the observed increases downgradient in the No-Ethanol Lane in an area where little growth substrate is present.

Observations of archaeal densities showed that elevated archaea were observed in the With-Ethanol Lane where sulfate was depleted [*Feris et al*., 2008]. After 244 days the measured archaea population increased about 3 orders of magnitude at the location of the injection wells in the With-Ethanol Lane (Fig. 12a). Simulations for that lane reproduced the observed growth of archaea from 10^3 to ~10^7 per mL copy numbers near the injection wells at 244 days. In contrast, in the No-Ethanol Lane field data did not show a significant growth of archaea above the background level (approximately 10^3 copy numbers per ml). Consistent with the measurements, our simulations indicated no methanogenesis occurring in the No-Ethanol Lane, hence no growth of archaea in this lane (Fig. 12d). The simulations could not produce the observed increase in archaea numbers between 152 and 244 days at 3-10 m downgradient because the ethanol substrate was consumed immediately downgradient of the injection well. As noted above, the difference may occur because the model simulates attached populations while the observations represent suspended cells.

Very few published studies have attempted to compare simulated to measured microbial data in a transient plume. *Essaid et al*. [1995] simulated aerobic and anaerobic biodegradation processes at the Bemidji, Minnesota, crude oil spill site and compared modeled and measured biomass only at the end of the simulation time (13 years). *Wilson et al*. [2012] developed a model based on results of active remediation of a BTEX plume but assumed a constant biomass. *Ma et al*. [2012] modeled microbial reactions and population dynamics at the fringe of a steady state plume using dual Monod kinetics to describe the microbial population dynamics. In a previous study, *Eckert and Appelo* [2002] simulated an *in situ* enhanced bioremediation of nitrate-contaminated aquifer with a well-pair

recirculation system using multi-Monod kinetics and biomass growth. However, they did not compare the modeled and field-measured biomass results. In this study, the simulations were somewhat successful in reproducing the order of magnitude of observed microbial population changes. Growth of SRB, total bacteria, and archaea were required to explain the transient behavior of the plume. The growth yields used for different populations were based either on theoretical values or were calibrated (Table 2). A comparison of the three calibrated values to theoretical values shows that the calibrated values used for growth yields of SRB and fermenters were reasonable, but the value for acetate-utilizing archaea was 10 times lower than the theoretical value (Table SI-2).

Models of reactive transport with biodegradation of multiple solutes coupled to biomass growth typically have a great many parameters, calling into question the validity of the calibrated values. In this study, the focus has been on process insights gained from incrementally revising the conceptual model, rather than on emphasizing the values obtained for the calibrated parameters. A general discussion of the calibrated values seems premature for several reasons. These include a paucity of other microbial datasets from transient field experiments, lack of consensus on the relationship between qPCR data and active populations, and questions on the relationship between attached and planktonic numbers. Instead we have concentrated on achieving simulated microbial growth at comparable orders of magnitude to the observations using reasonable growth yields. To assess which parameters were most important, the U.S. Geological Survey (USGS) universal inverse modeling code, UCODE_2005 [*Poeter et al*., 2005] was used to perform a sensitivity analysis for the calibrated parameters. The values of composite scaled sensitivity (CSS) are presented in Fig. SI-2. Interestingly, the archaea yield had the highest CSS and the calibrated value was low compared to the theoretical value (Table SI-2) suggesting that the archaea growth at this site is poorly understood. Other parameters with high sensitivities were the maximum specific growth rate of SRB ethanol degraders, sulfate half-saturation concentration, and maximum specific growth rate of SRB toluene degraders indicating the importance of methane production and sulfate reduction processes. A thorough examination of parameter sensitivities and correlation of parameters would be possible if more microbial datasets for these types of models become available.

Fig. 13 illustrates contour plots of the simulated plume for different compounds at 274 days, corresponding to the last observed data in the experiment. The benzene plume (defined here as concentrations greater than 20 μg/L) was about 4.5 times longer in the With-Ethanol Lane than in the No-Ethanol Lane by the end of the 274-day simulation time (Fig. 13a). Toluene and ethanol concentrations, which were non-detectable by this time are therefore not shown in Fig. 13. Simulated *o*-xylene persisted in the With-Ethanol Lane as was observed in the field [*Mackay et al*., 2006]. The methane concentrations (Fig. 13c) showed good agreement with the field observations although the simulated plume was somewhat shorter than the observed plume. The simulations of areal distributions of the microbial populations (Fig. 14) help identify zones within which active biodegradation under different redox conditions are to be expected. For example, Fig. 14b shows the area with high growth of total bacteria is also the area with active ethanol fermentation within the first 10 meters downgradient of the With-Ethanol Lane injection wells.

On the basis of simulated growth of archaea populations after 274 days, the methanogenic zone was found to have extended beyond 13 m downgradient of the ethanol injection source with the most active zone within 4 m downgradient from the ethanol injection source. The areas with high growth of microbial populations were consistent with observed redox processes from chemical data and can serve as an indicator of active biodegradation zones. Due to transport of dissolved methane with groundwater flow, identifying the methanogenic zone solely based on methane concentration is inaccurate.

5. Summary and Conclusions

A kinetics-based reactive transport model coupled to microbial growth was developed, providing quantitative understanding of the impact of ethanol and its degradation products on petroleum hydrocarbon compounds of interest: benzene (B), toluene (T), and *o*-xylene (*o*-X). High resolution data from a field study, intended to represent a small-volume release of E10 gasohol (10% ethanol and 90% conventional gasoline), were used to construct the model and identify important processes controlling the natural attenuation of different compounds.

Using insights from the field experiment, we included in our numerical model the degradation of BT*o*X under sulfate reduction and iron reduction, degradation of ethanol under sulfate reduction, iron reduction, and methanogenesis, and anaerobic oxidation of dissolved methane coupled sulfate and iron. Results reproduced the field observation that the natural attenuation of BT*o*X compounds was slowed significantly in the presence of dissolved-phase ethanol. The model results were also consistent with the observation that ethanol did not persist in the aquifer more than 0.5 meters downgradient of the injection wells. Discrepancies between simulations and the measured BT*o*X and ethanol data suggested that addition of iron reduction as a degradation pathway was a necessary refinement of the model. Also, since measurements indicated that sulfate was depleted to no lower than about 10 to 15 mg/L within the methanogenic zone, the model was further refined to account for this, an assumption supported by results of prior research by others. Modeling results indicated that vertical dispersion and diffusion of sulfate-rich groundwater from aquitard layers into the aquifer replenished the sulfate-depleted groundwater. Therefore, some BT*o*X compounds for which degradation under methanogenic conditions was limited were biodegraded by either iron- or sulfate-reduction further downgradient.

Based on field results, dissolved methane seemed to degrade with a constant rate over time, so the rate was assumed constant in the model. The model predicted methane concentrations in excess of the water solubility limit suggesting that a fraction of the generated methane escaped the groundwater. Simulations also suggested anaerobic oxidation of methane is required to explain methane data over time along the plume centerline. Another highlight of this study was that theoretical computed and calibrated bacteria yields resulted in microbial growth over time that matched reasonably well with observations. The model yield for archaea was too low by a factor of ten indicating that more work is needed to understand growth of the archaea populations under such conditions. In creating a model that reproduced the data for this field setting and experimental conditions it was necessary to use some phenomenological components based on observations. These include thresholds for ethanol and sulfate, negligible growth for iron reducers and methanogens on BT*o*X, and methane oxidation coupled to iron reduction. We have tried to document and discuss these assumptions so that future modeling efforts for other sites and conditions can examine whether the same effects occur and possibly advance methods for modeling the underlying mechanisms.

Acknowledgments

The project described was supported by Grant 2010–104864 from the American Petroleum Institute (API) and Award Number P42ES004699 from the National Institute of Environmental Health Sciences. The content is solely the responsibility of the authors and does not necessarily represent the official views of the National Institute of Environmental Health Sciences or the National Institutes of Health. Additional support was provided by the University Consortium for Field Focused Groundwater Contamination Research.

References

Adair, C.; Wilson, JT. Site Characterization of Ethanol-Blended Fuel Releases. National Tanks Conference; St Louis, MO. March 20, 2012; 2012. Available online at http://www.neiwpcc.org/tanksconference/presentations/Tuesday%20Presentations/Wilson_Adair_Site%20Characterization_Tuesday.pdf, edited

Amos RT, Mayer KU, Bekins BA, Delin GN, Williams RL. Use of dissolved and vapor-phase gases to investigate methanogenic degradation of petroleum hydrocarbon contamination in the subsurface. Water Resour Res. 2005; 41(2):W02001.

Amos RT, Bekins BA, Cozzarelli IM, Voytek MA, Kirshtein JD, Jones EJP, Blowes DW. Evidence for iron-mediated anaerobic methane oxidation in a crude oil-contaminated aquifer. Geobiology. 2012:n/a–n/a.

Anderson RT, Lovley DR. Anaerobic Bioremediation of Benzene under Sulfate-Reducing Conditions in a Petroleum-Contaminated Aquifer. Environmental Science & Technology. 2000; 34(11):2261–2266.

Beal EJ, House CH, Orphan VJ. Manganese- and Iron-Dependent Marine Methane Oxidation. Science. 2009; 325(5937):184–187. [PubMed: 19589998]

Bekins BA, Godsy EM, Goerlitz DF. Modeling Steady-State Methanogenic Degradation of Phenols in Groundwater. J Contam Hydrol. 1993; 14(3-4):279–294.

Bekins BA, Godsy EM, Warren E. Distribution of microbial physiologic types in an aquifer contaminated by crude oil. Microbial Ecol. 1999; 37(4):263–275.

Caldwell SL, Laidler JR, Brewer EA, Eberly JO, Sandborgh SC, Colwell FS. Anaerobic Oxidation of Methane: Mechanisms, Bioenergetics, and the Ecology of Associated Microorganisms. Environmental Science & Technology. 2008; 42(18):6791–6799. [PubMed: 18853791]

Cápiro NL, Da Silva MLB, Stafford BP, Rixey WG, Alvarez PJJ. Microbial community response to a release of neat ethanol onto residual hydrocarbons in a pilot-scale aquifer tank. Environmental Microbiology. 2008; 10(9):2236–2244. [PubMed: 18484998]

Chen YD, Barker JF, Gui L. A strategy for aromatic hydrocarbon bioremediation under anaerobic conditions and the impacts of ethanol: A microcosm study. J Contam Hydrol. 2008; 96(1–4):17–31. [PubMed: 17964687]

Clement T, Sun Y, Hooker B, Petersen J. Modeling Multispecies Reactive Transport in Ground Water. Ground Water Monitoring & Remediation. 1998; 18(2):79–92.

Corseuil HX, Hunt CS, Dos Santos RCF, Alvarez PJJ. The influence of the gasoline oxygenate ethanol on aerobic and anaerobic BTX biodegradation. Water Res. 1998; 32(7):2065–2072.

Corseuil HX, Monier AL, Fernandes M, Schneider MR, Nunes CC, do Rosario M, Alvarez PJJ. BTEX Plume Dynamics Following an Ethanol Blend Release: Geochemical Footprint and Thermodynamic Constraints on Natural Attenuation. Environmental Science & Technology. 2011; 45(8):3422–3429. [PubMed: 21410252]

Crowe SA, et al. The methane cycle in ferruginous Lake Matano. Geobiology. 2011; 9(1):61–78. [PubMed: 20854329]

Davis GB, Barber C, Power TR, Thierrin J, Patterson BM, Rayner JL, Wu Q. The variability and intrinsic remediation of a BTEX plume in anaerobic sulphate-rich groundwater. J Contam Hydrol. 1999; 36(3–4):265–290.

Deeb RA, Sharp JO, Stocking A, McDonald S, West KA, Laugier M, Alvarez PJJ, Kavanaugh MC, Alvarez-Cohen L. Impact of ethanol on benzene plume lengths: Microbial and modeling studies. J Environ Eng-Asce. 2002; 128(9):868–875.

Dolfing J. The microbial logic behind the prevalence of incomplete oxidation of organic compounds by acetogenic bacteria in methanogenic environments. Microbial Ecol. 2001; 41(2):83–89.

Eckert P, Appelo CAJ. Hydrogeochemical modeling of enhanced benzene, toluene, ethylbenzene, xylene (BTEX) remediation with nitrate. Water Resour Res. 2002; 38(8):1130.

EPA. EPA On-line Tools for Site Assessment Calculation, edited, United States Environmental Protection Agency (US EPA). 2011 Jan. http://www.epa.gov/athens/learn2model/part-two/onsite/estdiffusion.html

Essaid HI, Bekins BA, Godsy EM, Warren E, Baedecker MJ, Cozzarelli IM. Simulation of aerobic and anaerobic biodegradation processes at a crude oil spill site. Water Resour Res. 1995; 31(12):3309–3327.

Feris K, Mackay D, de Sieyes N, Chakraborty I, Einarson M, Hristova K, Scow K. Effect of ethanol on microbial community structure and function during natural attenuation of benzene, toluene, and o-xylene in a sulfate-reducing aquifer. Environmental Science & Technology. 2008; 42(7):2289–2294. [PubMed: 18504955]

Freitas JG, Fletcher B, Aravena R, Barker JF. Methane Production and Isotopic Fingerprinting in Ethanol Fuel Contaminated Sites. Ground Water. 2010; 48(6):844–857. [PubMed: 20070380]

Freitas JG, Mocanu MT, Zoby JLG, Molson JW, Barker JF. Migration and fate of ethanol-enhanced gasoline in groundwater: A modelling analysis of a field experiment. J Contam Hydrol. 2011; 119(1–4):25–43. [PubMed: 20869788]

Gomez DE, de Blanc PC, Rixey WG, Bedient PB, Alvarez PJJ. Modeling benzene plume elongation mechanisms exerted by ethanol using RT3D with a general substrate interaction module. Water Resour Res. 2008; 44(5)

Harbaugh, AW.; Banta, ER.; Hill, MC.; McDonald, MG. Rep. U.S. Geological Survey Open-File Report 00-92; 2000. MODFLOW-2000, the U.S. Geological Survey modular ground-water model -- User guide to modularization concepts and the Ground-Water Flow Process; p. 121

Harvey RW, Barber LB. Associations of Free-Living Bacteria and Dissolved Organic-Compounds in a Plume of Contaminated Groundwater. J Contam Hydrol. 1992; 9(1-2):91–103.

ITRC. Interstate Technology & Regulatory Council, Biofuel Team; Washington, DC, USA: 2011. Biofuels: Release Prevention, Environmental Behavior, and Remediation. http://www.itrcweb.org/documents/biofuels/biofuels-1.pdf

Klappenbach JA, Saxman PR, Cole JR, Schmidt TM. rrndb: the Ribosomal RNA Operon Copy Number Database. Nucleic Acids Res. 2001; 29(1):181–184. [PubMed: 11125085]

Knab NJ, Dale AW, Lettmann K, Fossing H, Jørgensen BB. Thermodynamic and kinetic control on anaerobic oxidation of methane in marine sediments. Geochim Cosmochim Ac. 2008; 72(15): 3746–3757.

Lee EJ, Kim M, Kim Y, Lee K-K. Numerical and field investigation of enhanced in situ denitrification in a shallow-zone well-to-well recirculation system. Ecological Modelling. 2009; 220(19):2441–2449.

Leloup J, Loy A, Knab NJ, Borowski C, Wagner M, Jørgensen BB. Diversity and abundance of sulfate-reducing microorganisms in the sulfate and methane zones of a marine sediment, Black Sea. Environmental Microbiology. 2007; 9(1):131–142. [PubMed: 17227418]

Lovanh N, Hunt CS, Alvarez PJJ. Effect of ethanol on BTEX biodegradation kinetics: aerobic continuous culture experiments. Water Res. 2002; 36(15):3739–3746. [PubMed: 12369521]

Ma J, Rixey WG, DeVaull GE, Stafford BP, Alvarez PJJ. Methane Bioattenuation and Implications for Explosion Risk Reduction along the Groundwater to Soil Surface Pathway above a Plume of Dissolved Ethanol. Environmental Science & Technology. 2012; 46(11):6013–6019. [PubMed: 22568485]

Mackay DM, Einarson MD, Kaiser PM, Nozawa-Inoue M, Goyal S, Chakraborty I, Rasa E, Scow KM. Mass Discharge in a Tracer Plume: Evaluation of the Theissen Polygon Method. Ground Water. 2012; 50(6):895–907. [PubMed: 22324777]

Mackay DM, et al. Impact of Ethanol on the Natural Attenuation of Benzene, Toluene, and o-Xylene in a Normally Sulfate-Reducing Aquifer. Environmental Science & Technology. 2006; 40(19): 6123–6130. [PubMed: 17051810]

Martens CS, Berner RA. Interstitial Water Chemistry of Anoxic Long Island Sound Sediments. 1. Dissolved Gases. Limnology and Oceanography. 1977; 22(1):10–25.

Molson JW, Barker JF, Frind EO, Schirmer M. Modeling the impact of ethanol on the persistence of benzene in gasoline-contaminated groundwater. Water Resour Res. 2002; 38(1)

Molz FJ, Widdowson MA, Benefield LD. Simulation of Microbial-Growth Dynamics Coupled to Nutrient and Oxygen-Transport in Porous-Media. Water Resour Res. 1986; 22(8):1207–1216.

Monod J. The Growth of Bacterial Cultures. Annu Rev Microbiol. 1949; 3:371–394.

Nelson DK, LaPara TM, Novak PJ. Effects of Ethanol-Based Fuel Contamination: Microbial Community Changes, Production of Regulated Compounds, and Methane Generation. Environmental Science & Technology. 2010; 44(12):4525–4530. [PubMed: 20481624]

NRC. Natural attenuation for groundwater remediation National Research Council (U S) Committee on Intrinsic Remediation. Vol. xiv. National Academy Press; Washington, D.C: 2000. p. 274

Poeter, EP.; Hill, MC.; Banta, ER.; Mehl, S.; Christensen, S. Rep. U.S. Geological Survey Techniques and Methods 6-A11; 2005. UCODE_2005 and Six Other Computer Codes for Universal Sensitivity Analysis, Calibration, and Uncertainty Evaluation; p. 283

Postma D, Jakobsen R. Redox zonation: Equilibrium constraints on the Fe(III)/SO4-reduction interface. Geochim Cosmochim Ac. 1996; 60(17):3169–3175.

Powers SE, Hunt CS, Heermann SE, Corseuil HX, Rice D, Alvarez PJJ. The transport and fate of ethanol and BTEX in groundwater contaminated by gasohol. Crit Rev Env Sci Tec. 2001; 31(1): 79–123.

Rasa, E. PhD Dissertation. Department of Civil and Environmental Engineering, University of California; Davis, California, USA: 2012. Impacts of Back Diffusion and Biodegradation on MTBE/TBA Plumes and Impacts of Spills of Ethanol-Blended Biofuels on Groundwater: Development of Models for Evaluating Field Experiments and Their Implications.

Rasa E, Foglia L, Mackay DM, Scow KM. Effect of different transport observations on inverse modeling results: Case study of a long term groundwater tracer test monitored at high resolution. Hydrogeol J. 2013 In Press.

Rasa E, Chapman SW, Bekins BA, Fogg GE, Scow KM, Mackay DM. Role of back diffusion and biodegradation reactions in sustaining an MTBE/TBA plume in alluvial media. J Contam Hydrol. 2011; 126(3-4):235–247. [PubMed: 22115089]

Regnier P, Dale AW, Arndt S, LaRowe DE, Mogollon J, Van Cappellen P. Quantitative analysis of anaerobic oxidation of methane (AOM) in marine sediments: A modeling perspective. Earth-Sci Rev. 2011; 106(1-2):105–130.

Rittmann, BE.; McCarty, PL. Environmental biotechnology : principles and applications. Vol. xiv. McGraw-Hill; Boston: 2001. p. 754

Roychoudhury A, McCormick D. Kinetics of Sulfate Reduction in a Coastal Aquifer Contaminated with Petroleum Hydrocarbons. Biogeochemistry. 2006; 81(1):17–31.

Roychoudhury AN, Van Cappellen P, Kostka JE, Viollier E. Kinetics of microbially mediated reactions: dissimilatory sulfate reduction in saltmarsh sediments (Sapelo Island, Georgia, USA). Estuarine, Coastal and Shelf Science. 2003; 56(5–6):1001–1010.

Scheidegger A. General Theory of Dispersion in Porous Media. J Geophys Res. 1961; 66(10):3273–3278.

Spalding RF, Toso MA, Exner ME, Hattan G, Higgins TM, Sekely AC, Jensen SD. Long-Term Groundwater Monitoring Results at Large, Sudden Denatured Ethanol Releases. Ground Water Monitoring & Remediation. 2011; 31(3):69–81.

Suflita JM, Mormile MR. Anaerobic Biodegradation of Known and Potential Gasoline Oxygenates in the Terrestrial Subsurface. Environmental Science & Technology. 1993; 27(5):976–978.

Wilson, JT.; Toso, MA.; Mackay, DM.; de Sieyes, N.; DeVaull, GE. L U S T Line: A Report on Federal & State Programs to Control Leaking Underground Storage Tanks. Vol. 71. The New England Interstate Water Pollution Control Commission; Lowell Massachusetts: 2012 Sep. What's the Deal with Methane at LUST Spill Sites?; p. 6-8.

Wood, I. Master's thesis. University of California; Davis: 2004. Assessment of Potential Impacts of the Fuel Oxygenate Ethanol on the Natural Attenuation of BTEX and MTBE at Vandenberg Air Force Base, California.

Annotation*

Fundamental quantities

B benzene concentration (mg/L)

T	toluene concentration (mg/L)
X	*o*-xylene concentration (mg/L)
EtOH	ethanol concentration (mg/L)
SO_4	sulfate concentration (mg/L)
Fe^{+3}	sediment iron concentration (mg/kg)
Acet	acetate concentration (mg/L)
CH_4	dissolved methane concentration (mg/L)
S_1	BT*o*X-degrading iron-reducing bacteria (mg/L)
S_2	BT*o*X-degrading sulfate-reducing bacteria (mg/L)
S_3	ethanol-degrading iron-reducing bacteria (mg/L)
S_4	ethanol-degrading sulfate-reducingbacteria (mg/L)
S_5	fermentative bacteria(mg/L)
S_6	acetate-degrading archaea (mg/L)

Kinetic parameters

R	reaction rate (mg/L/day)
R_{max}	maximum degradation rate (mg/L/day)
μ_S	maximum specific growth rate (1/day)
Y_S	biomass yield coefficient
Y	mass ratio of different solutes
K	half-saturation concentration (mg/L)
K^i	inhibition concentration (mg/L)
b_S	biomass decay rate (1/day)
f_{EtoH}	Flag for BT*o*X degradation inhibition in the presence of ethanol (-)
f_{SO_4}	Flag for limiting sulfate reduction when sulfate is less than a threshold (-)

* The specific parameters and their values are listed in Table 2.

Key Points

- Reactive transport model fits data from anaerobic field experiment with ethanol and BTEX species
- Microbial growth simulations reproduce observations of sulfate reducers, fermenters and methanogens
- Simulations suggest methane degradation is coupled to sulfate and iron reduction

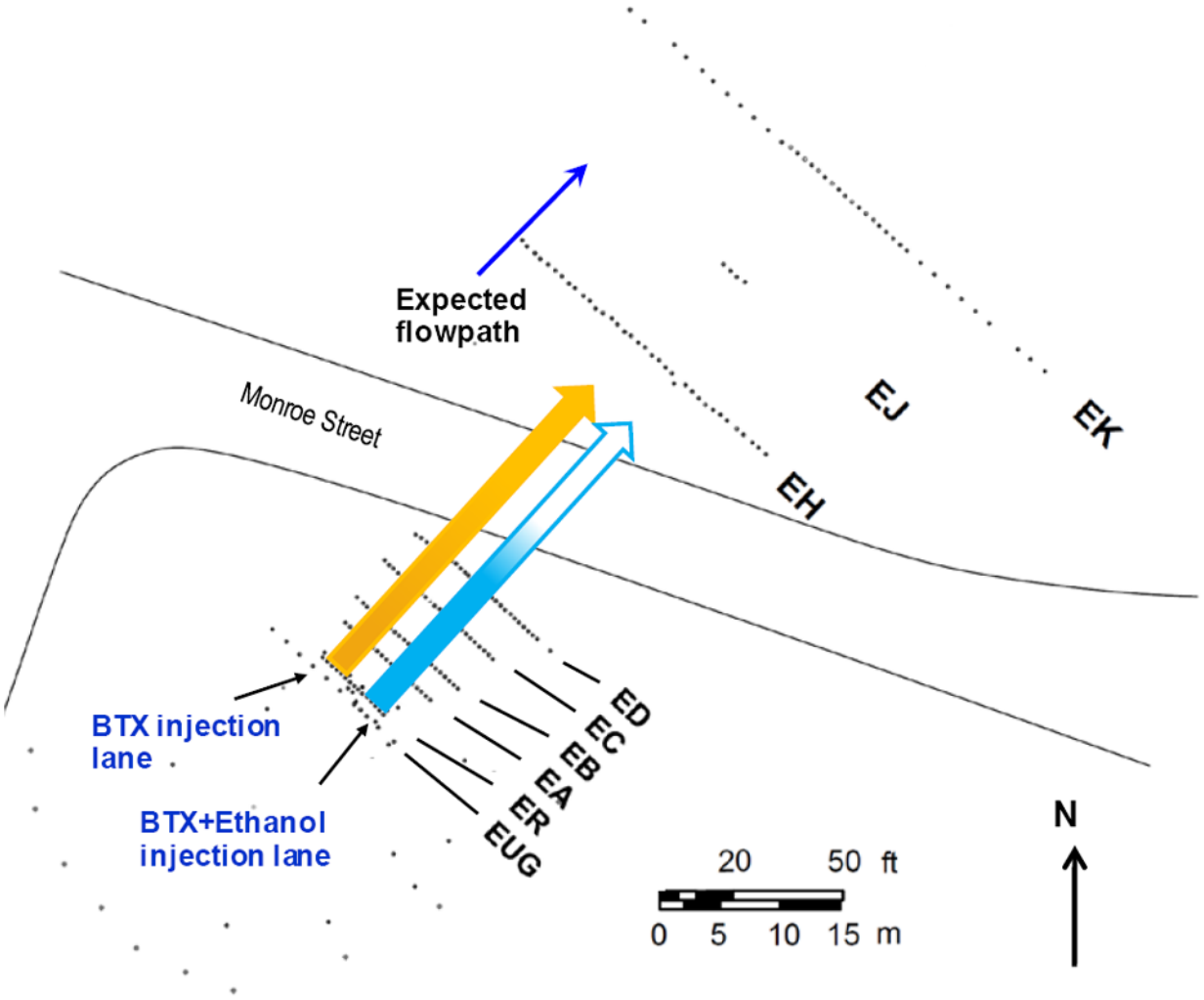

Figure 1.
Map of Site 60, Vandenberg Air Force Base (VAFB) in California. Groundwater from upgradient of the wells was spiked with BT*o*X (No-Ethanol Lane on the west side) and with BT*o*X+ethanol (With-Ethanol Lane on the east side). Spiked groundwater was injected in the ER wells to create two side-by-side plumes.

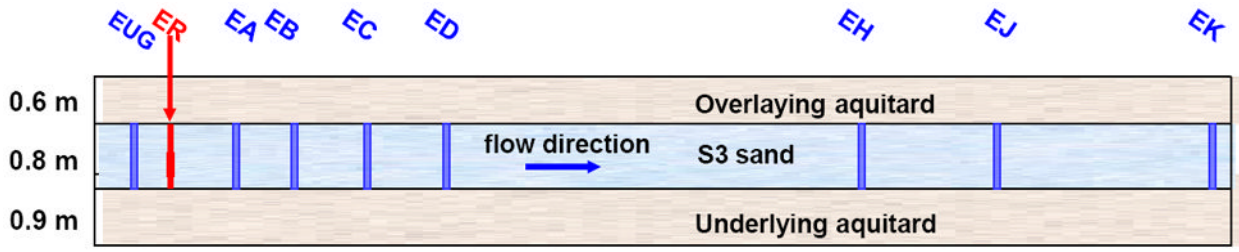

Figure 2.
Conceptual subsurface model and layering used for this study. Model domain is quasi-3D with homogenous saturated horizontal layers, as shown. The ER wells were used to inject the BT*o*X and ethanol compounds into the S3 sand aquifer (Fig. 1). Diagram is not to scale.

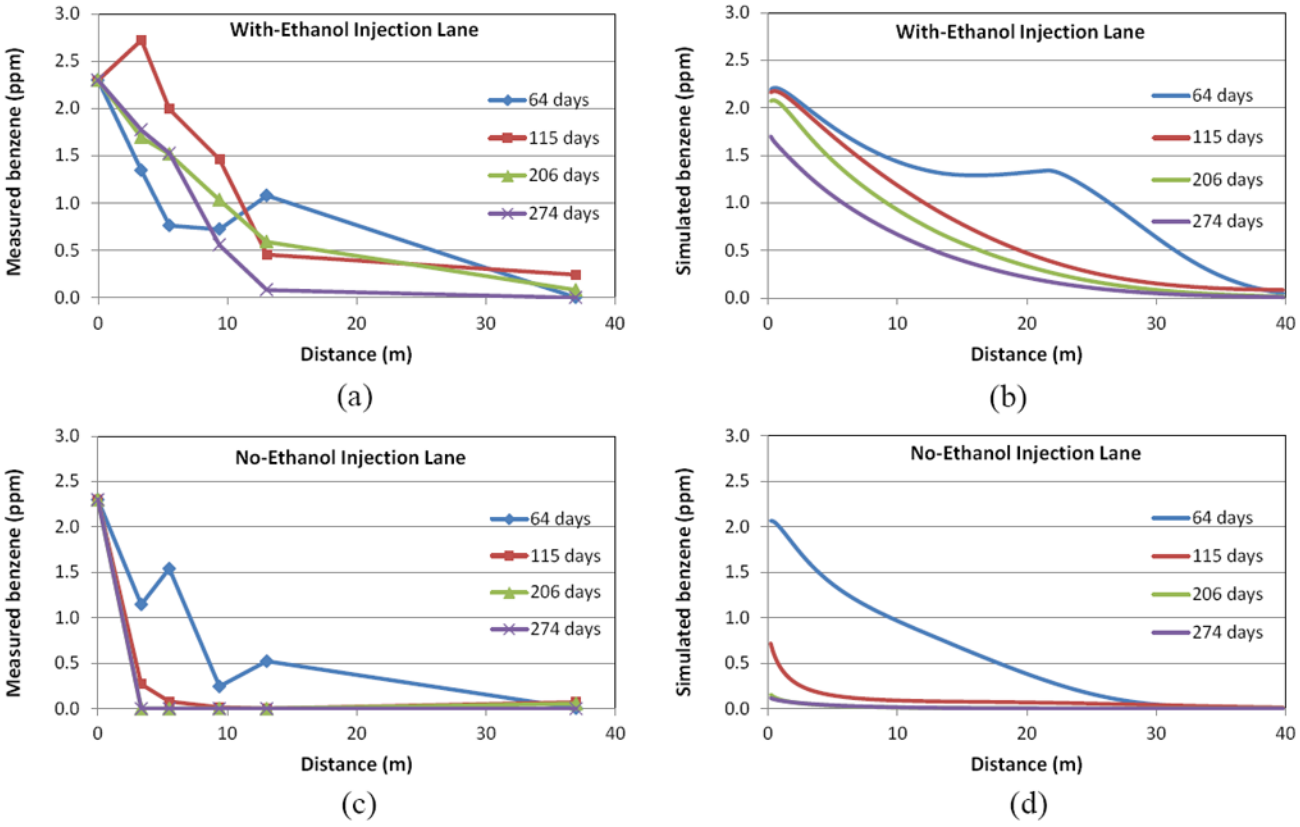

Figure 3.
Comparison of measured (left panels) versus simulated benzene (right panels) concentrations in the centerline of the With-Ethanol (a and b) and No-Ethanol experimental lanes (c and d). Benzene injection concentration was used as measured concentration in groundwater at distance=0 (a and c).

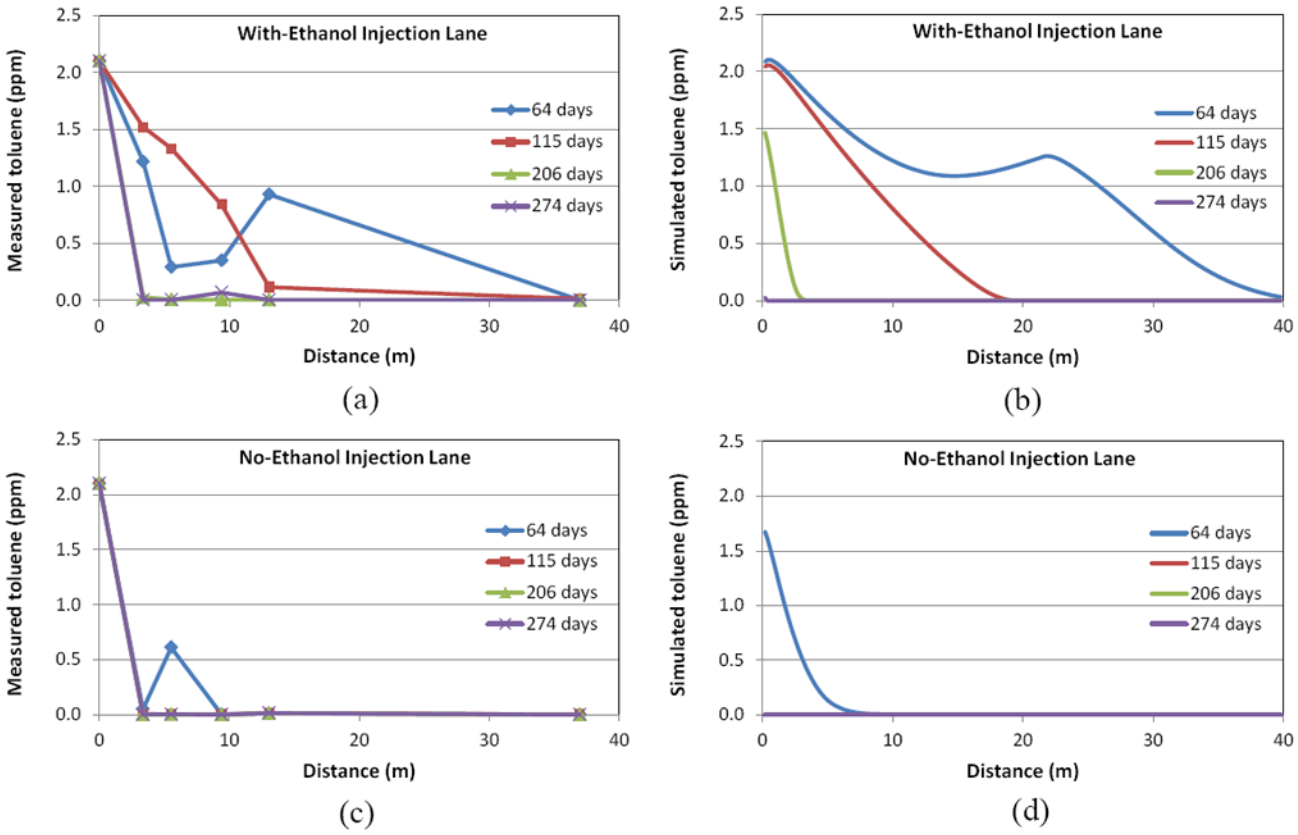

Figure 4.

Comparison of measured (left panels) versus simulated toluene (right panels) concentrations in the centerline of the With-Ethanol (a and b) and No-Ethanol experimental lanes (c and d). Toluene injection concentration was used as measured concentration in groundwater at distance=0 (a and c).

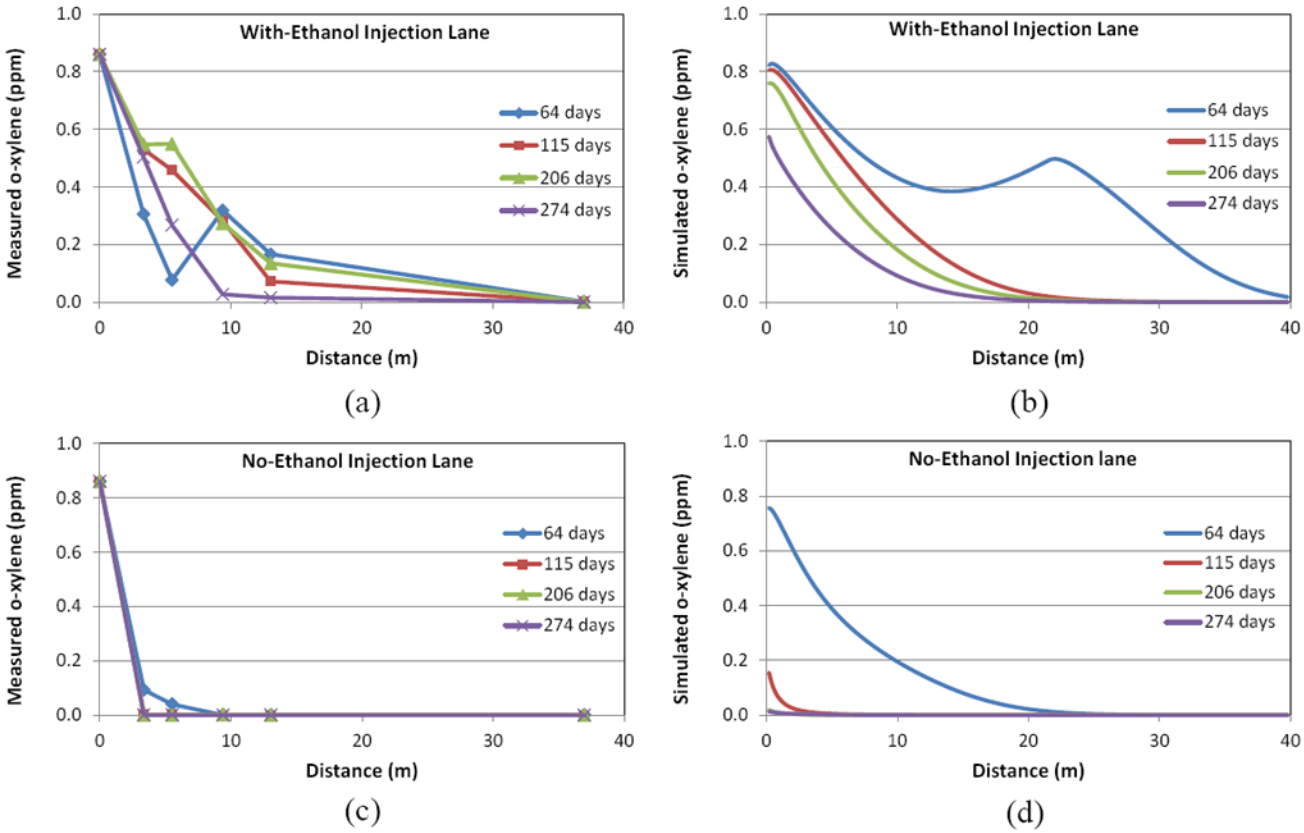

Figure 5.

Comparison of measured (left panels) versus simulated *o*-xylene (right panels) concentrations in the centerline of the With-Ethanol (a and b) and without-ethanol experimental lanes (c and d). *O*-xylene injection concentration was used as measured concentration in groundwater at distance=0 (a and c).

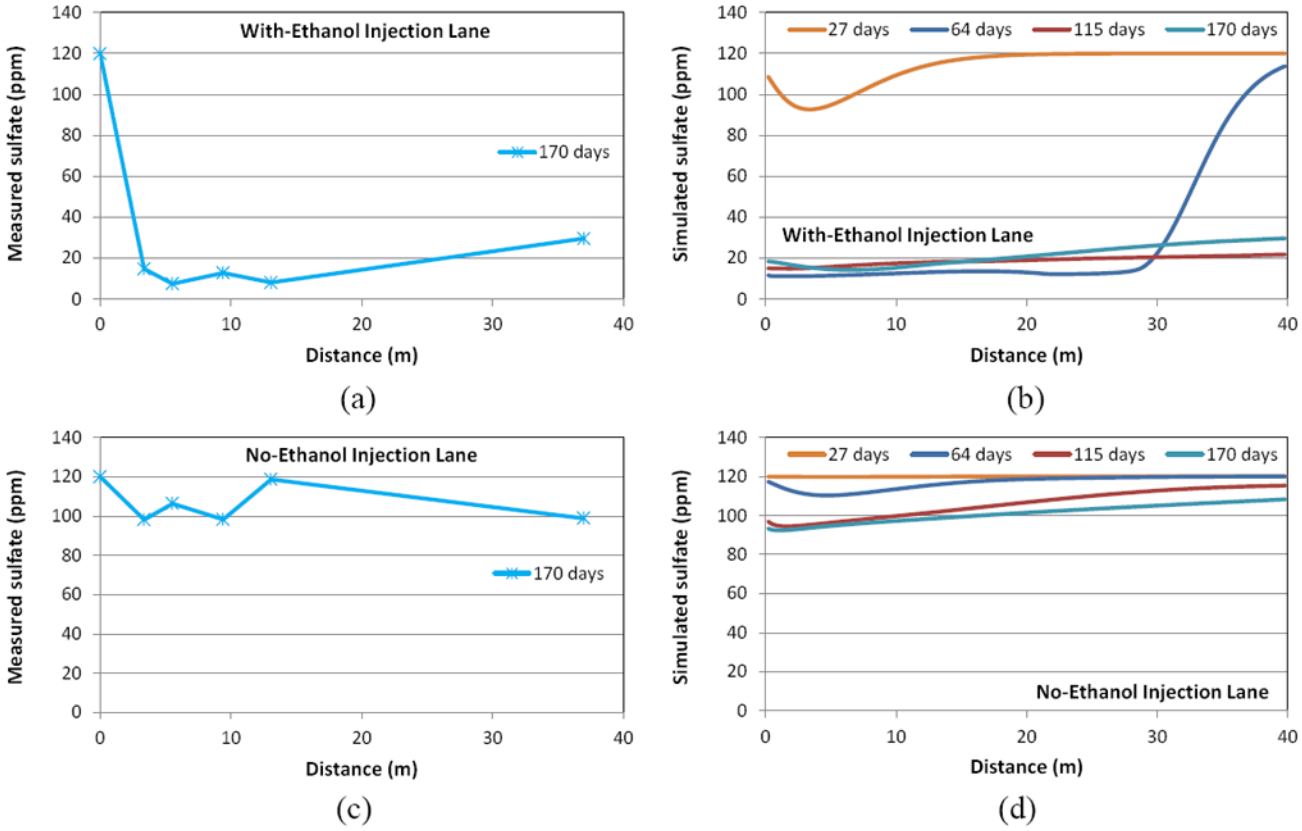

Figure 6.

Comparison of measured (left panels) versus simulated sulfate (right panels) concentrations in the centerline of the With-Ethanol (a and b) and No-Ethanol experimental lanes (c and d). Background sulfate concentration was used as measured concentration in groundwater at distance=0 (a and c).

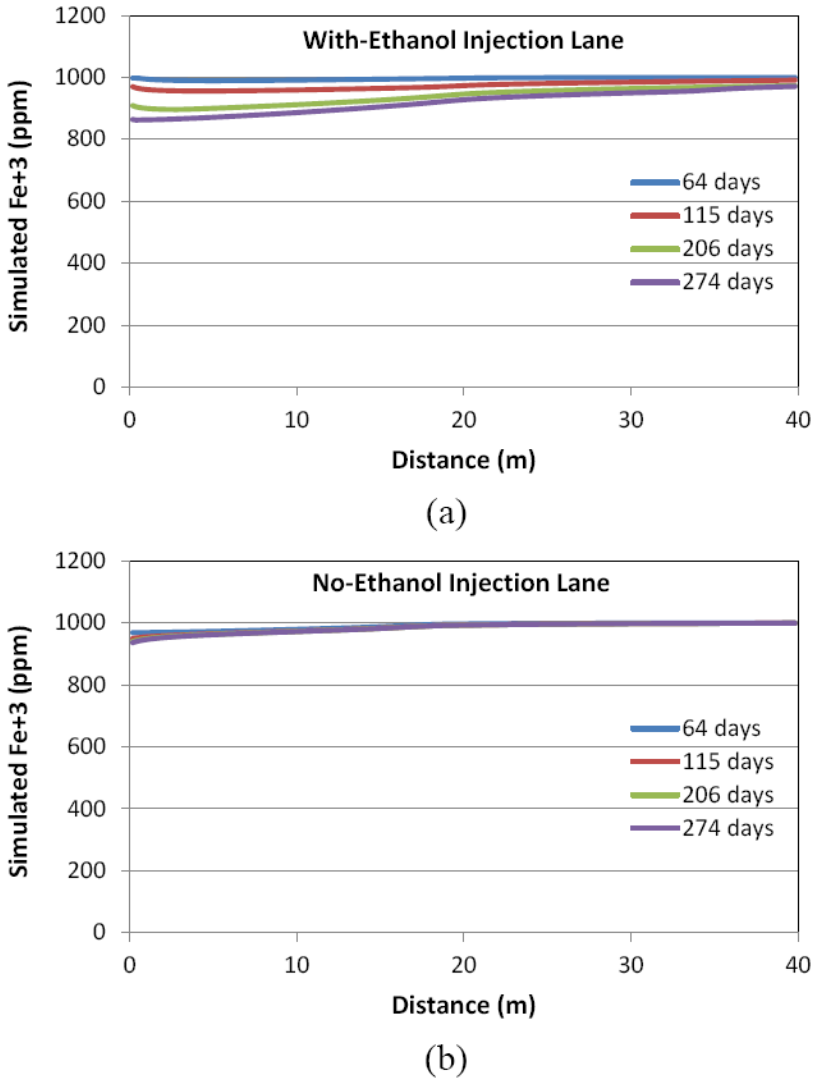

Figure 7.
Simulated ferric iron concentrations in the centerline of the With-Ethanol Lane. Note that there were no measurements made during the field experiment.

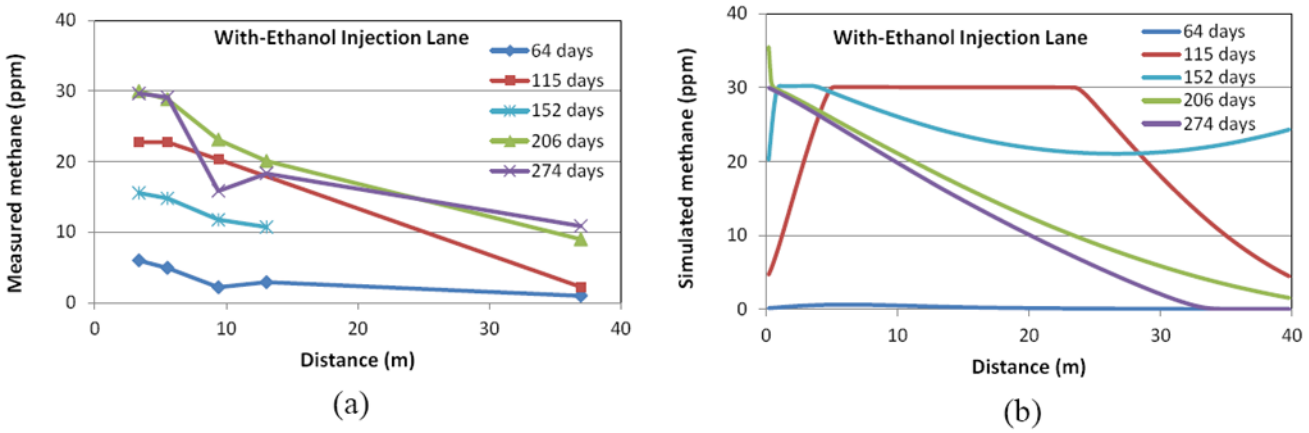

Figure 8.
Comparison of measured (a) versus dissolved methane (b) concentrations in the centerline of the With-Ethanol Lane.

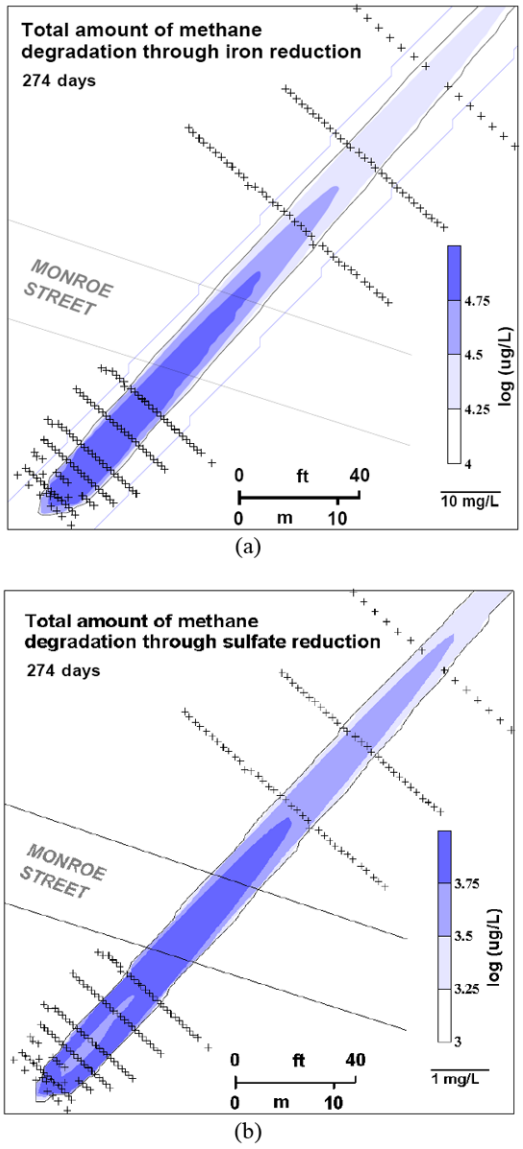

Figure 9.
Total amount of methane oxidation through iron reduction (a) and sulfate reduction (b) over the 283 days of simulation.

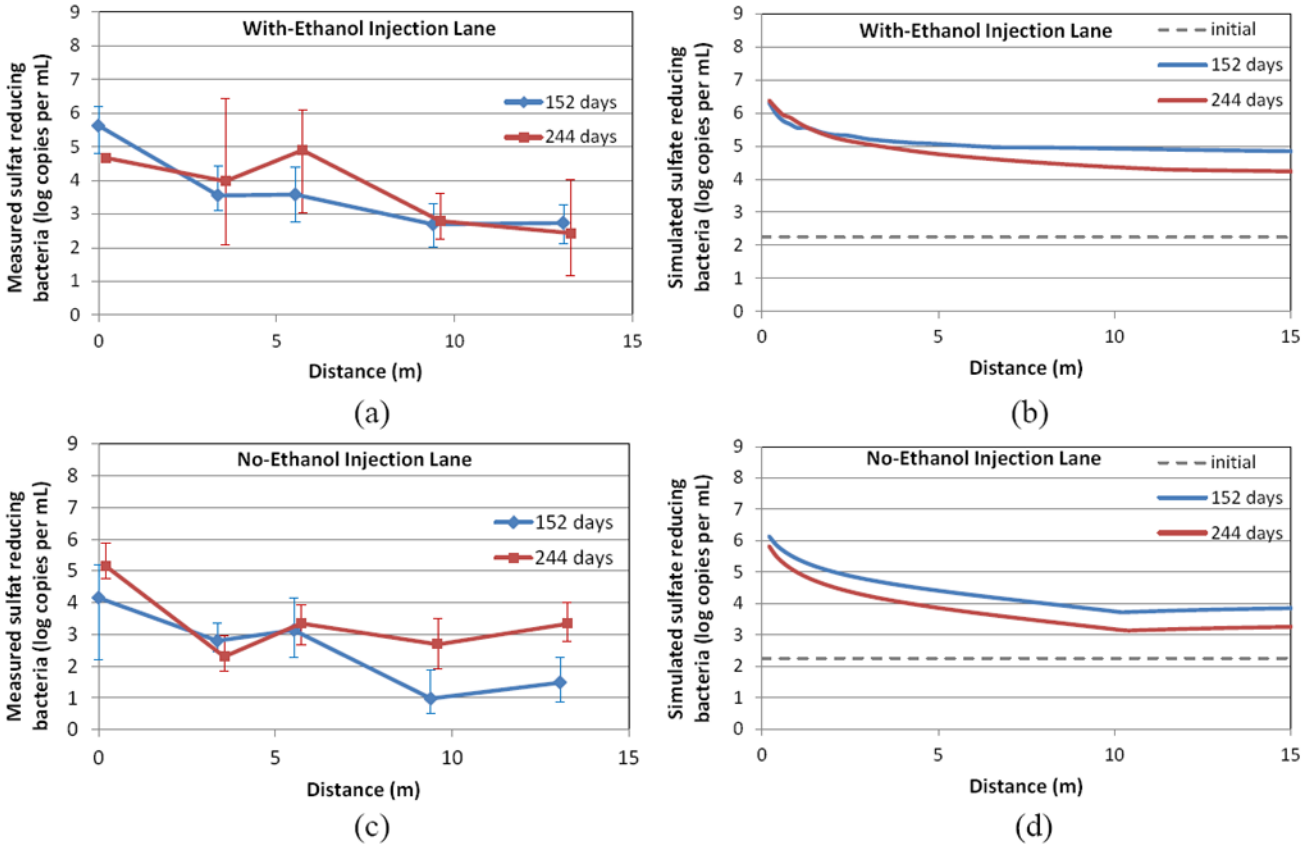

Figure 10.

Comparison of measured (left panels) versus simulated sulfate-reducing bacteria (right panels) densities in the centerline of the With-Ethanol (a and b) and No-Ethanol experimental lanes (c and d). The dashed line represents the background populations at the site estimated from monitoring data in areas unaffected by the experimental injections. Upper and lower whiskers represent maximum and minimum of sampling wells from the center of the experimental lanes, respectively. Results of 244-day data are plotted at slightly offset distances for clarity.

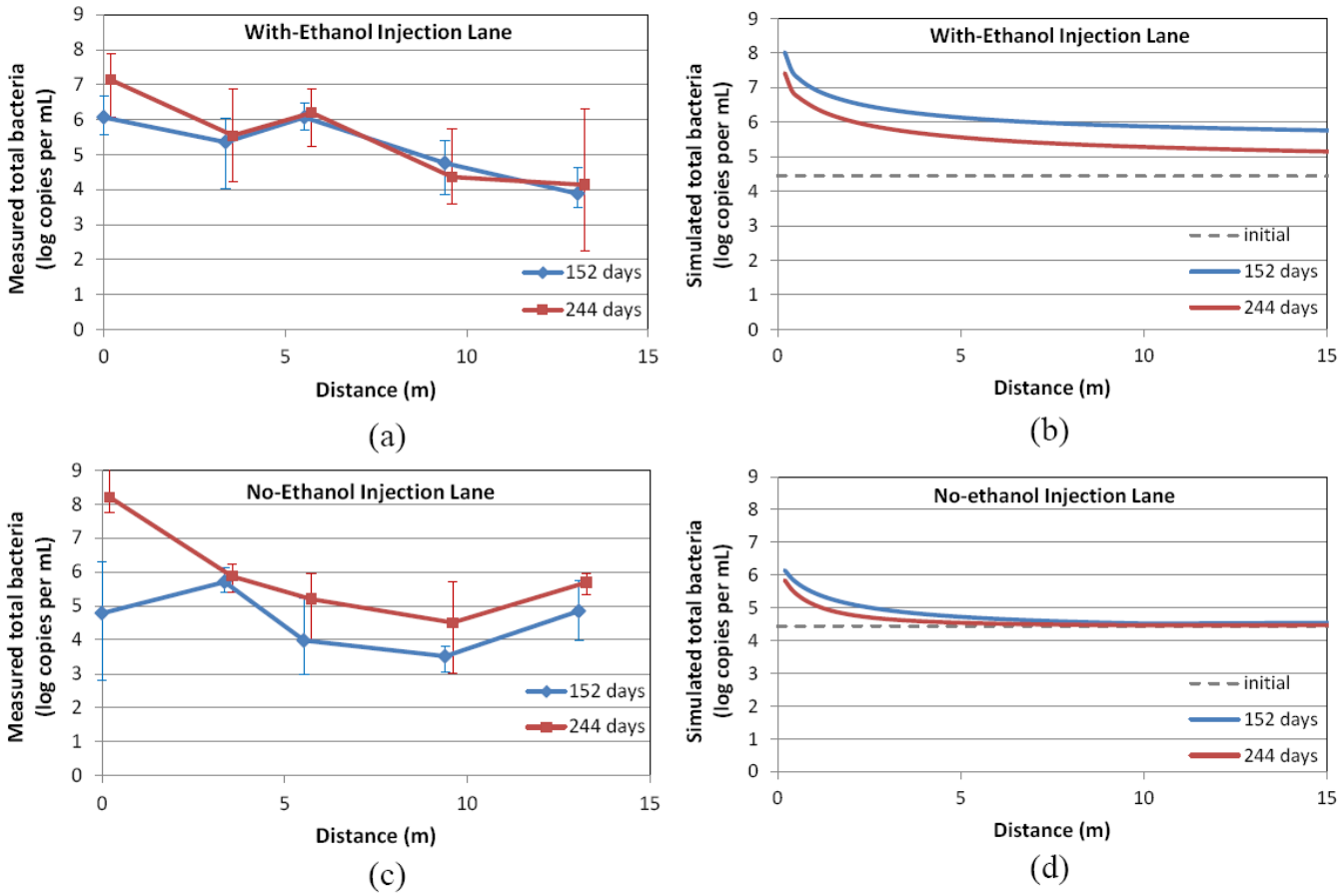

Figure 11.

Comparison of measured (left panels) versus simulated total bacteria (right panels) densities in the centerline of the With-Ethanol (a and b) and No-Ethanol experimental lanes (c and d). The dashed line represents the background level at the site estimated based on data from area unaffected by the plume. Upper and lower whiskers represent maximum and minimum of sampling wells from the center of the experimental lanes, respectively. Results of 244-day data are plotted at slightly offset distances for clarity.

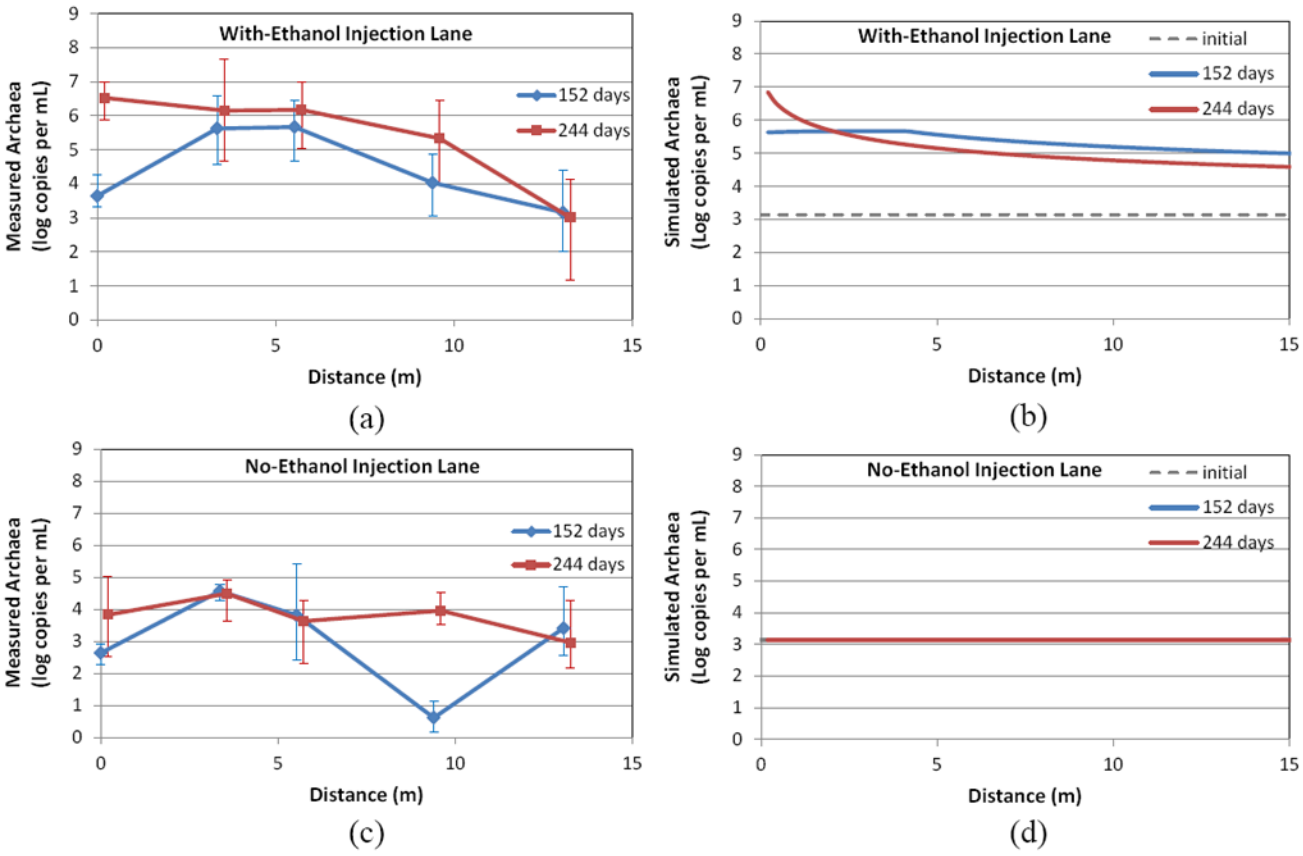

Figure 12.

Comparison of measured (left panels) versus simulated archaea (right panels) densities in the centerline of the With-Ethanol (a and b) and No-Ethanol experimental lanes (c and d). Dashed line represents the background level at the site estimated based on data from the areas unaffected by the plume. Upper and lower whiskers represent maximum and minimum of sampling wells from the center of the experimental lanes, respectively. Results of 244-day data are plotted at slightly offset distances for clarity.

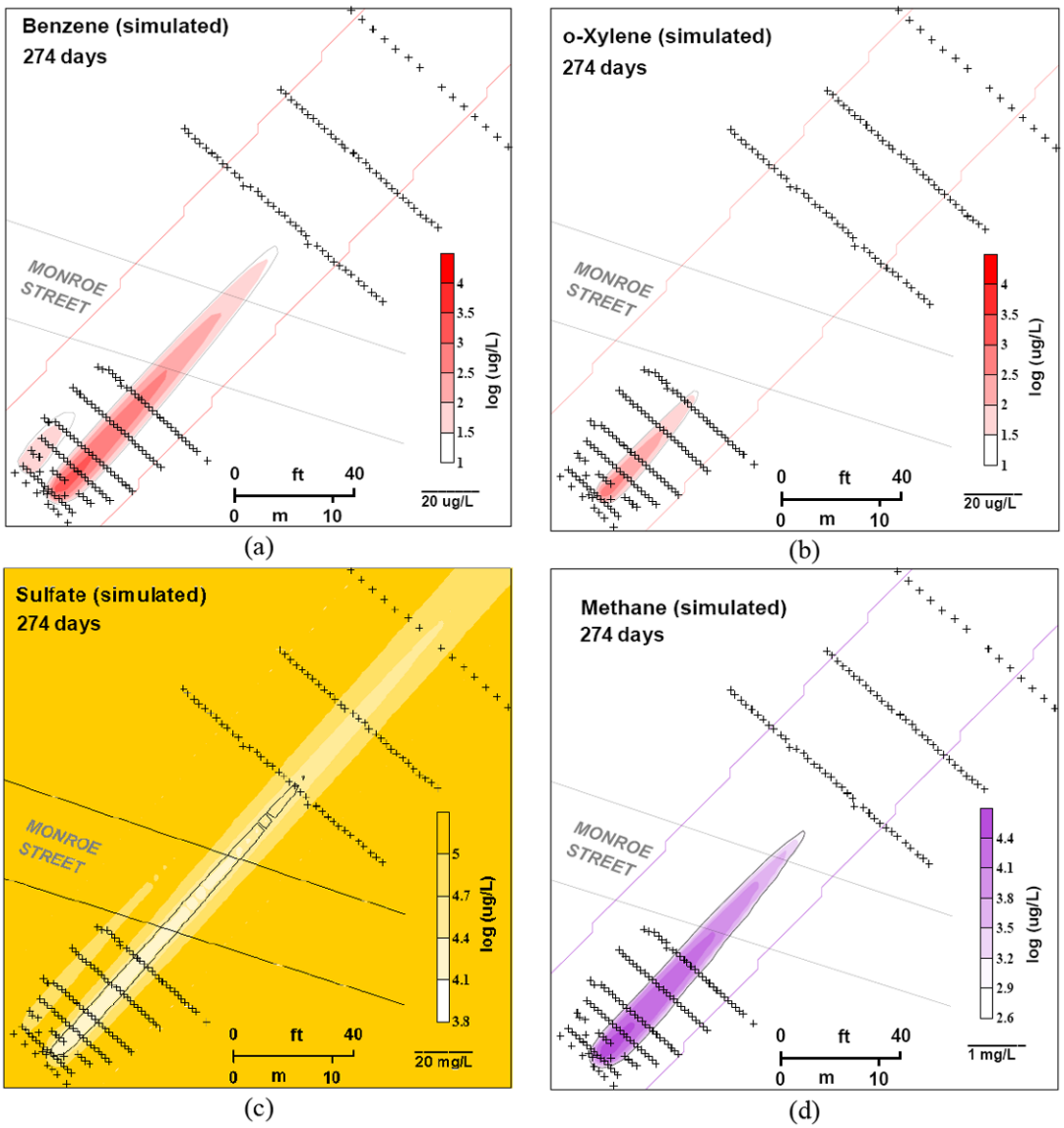

Figure 13.

Simulated plumes of different compounds in the No-Ethanol Lane (west side) and the With-Ethanol Lane (east side) after 274 days of the experiment for benzene (a), *o*-xylene (b), sulfate (c), and dissolved methane (d). For the location of injection wells within each experimental lane refer to Fig. 1. There was no detectable toluene and ethanol in the simulations after 274 days therefore we do not show their contour plots here.

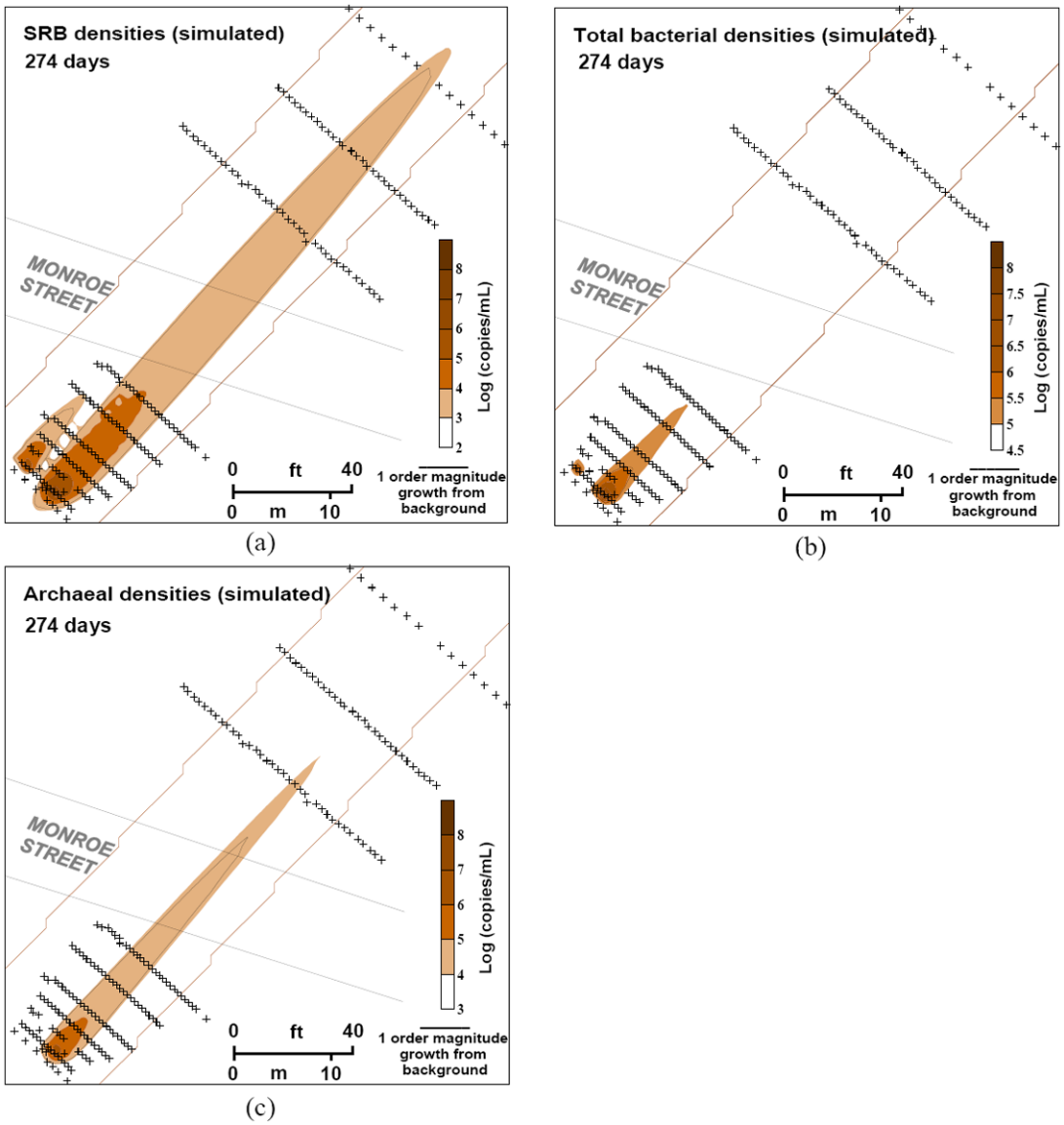

Figure 14.

Populations ofsulfate-reducing bacteria (a), total bacteria (b), and total archaea (c) simulated by the calibrated reactive transport model after 274 days. The initial densities based on background data were 1.7×10^2 for sulfate-reducing bacteria (SRB), 2.8×10^4 for the total bacteria, and 1.4×10^3 copies per mL of groundwater for archaea. Contour lines represent the area with one order of magnitude growth from the initial density.

Table 1

Parameters for the flow and transport model. See text for discussion and assumed locations.

Parameter	Value	Source
Hydraulic parameters		
Aquifer horizontal hydraulic conductivity	10.89 m/d	[*Rasa et al*., 2013][1]
Silt layers horizontal hydraulic conductivity	2×10^{-2} m/d	[*Rasa et al*., 2013][1]
Horizontal to vertical hydraulic conductivity ratio	10	assumed
Hydraulic gradient (i)	0.0132	[*Mackay et al*., 2012]
Aquifer effective porosity	0.34	[*Mackay et al*., 2012]
Silt layers effective porosity	0.4	[*Rasa et al*., 2011]
Injection rates	200 mL/min	[*Mackay et al*., 2006]
Transport parameters		
Retardation factor of benzene (Rf_B)	1.2	[*Mackay et al*., 2006]
Retardation factor of toluene (Rf_T)	1.6	[*Mackay et al*., 2006]
Retardation factor of *o*-xylene (Rf_X)	2.3	[*Mackay et al*., 2006]
Longitudinal dispersivity (α_L)	0.55 m	[*Rasa et al*., 2013][1]
Transverse horizontal dispersivity (α_T)	0.013 m	[*Rasa et al*., 2013][1]
Transverse vertical dispersivity (α_V)	1.3×10^{-3} m	[*Rasa et al*., 2013][1]
Benzene aqueous diffusion coefficient (D_{aq}) [2]	6.71×10^{-5} m^2/d	[*EPA*, 2011]
Tortuosity (τ)	0.40	[*Rasa et al*., 2011]
Background sulfate concentration	120 mg/L	[*Mackay et al*., 2006]
Background iron concentration	1,000 mg/kg	[*Wood*, 2004]
Initial density of BT*o*X-degrading iron-reducing bacteria (S_1) [3]	10^{-4} mg/L	Assumed same as S_2
Initial density of BT*o*X-degrading sulfate-reducingbacteria (S_2) [4]	10^{-4} mg/L	Calculated based on [*Feris et al*., 2008]
Initial density of Ethanol-degrading iron-reducing bacteria (S_3) [3]	10^{-4} mg/L	Assumed same as S_4
Initial density of Ethanol-degrading sulfate-reducing bacteria (S_4) [4]	10^{-4} mg/L	Calculated based on [*Feris et al*., 2008]
Initial density of Fermentative bacteria (S_5) [5]	0.0317 mg/L	Calculated based on [*Feris et al*., 2008]
Initial density of acetate-degrading archaea (S_6) [6]	0.0046 mg/L	Calculated based on [*Feris et al*., 2008]
Benzene injection concentration	2.3 mg/L	[*Mackay et al*., 2006]
Toluene injection concentration	2.2 mg/L	[*Mackay et al*., 2006]
o-Xylene injection concentration	0.87 mg/L	[*Mackay et al*., 2006]
Ethanol injection concentration	470 mg/L	[*Mackay et al*., 2006]

[1] Hydraulic conductivity and longitudinal and horizontal dispersivities were estimated by inverse modeling of long term tracer study at the site.

[2] RT3D model ver. 2.5 used here allows only one diffusion coefficient for the multispecies reactive transport as discussed in *Rasa et al*., [2011].

[3] Total iron-reducing bacteria (IRB) is S_1+S_3

[4] Total sulfate-reducing bacteria (SRB) is S_2+S_4

[5] Total bacteria is $S_1+S_2+S_3+S_4+S_5$

[6] Total archaea is S_6

Table 2

Kinetic parameter values

Symbol	Definition	Value	Source
$R_{SO_4}^{CH_4}$	Rate of anaerobic methane oxidation coupled to sulfate (mg/L/day)	0.04	Calibrated
$R_{Fe}^{CH_4}$	Rate of anaerobic methane oxidation coupled to iron (mg/L/day)	0.28	Calibrated
$R_{max_{Fe}}^{B}$	Maximum degradation rate of benzene coupled to iron (mg/L/day)	0.05	Calibrated
$R_{max_{Fe}}^{T}$	Maximum degradation rate of toluene coupled to iron (mg/L/day)	0.05	Calibrated
$R_{max_{Fe}}^{X}$	Maximum degradation rate of *o*-xylene coupled to iron (mg/L/day)	0.03	Calibrated
$\mu_{S_2}^{B}$	Maximum specific growth rate of SRB[a] benzene degraders (1/day)	0.045	Calibrated
$\mu_{S_2}^{T}$	Maximum specific growth rate of SRB toluene degraders (1/day)	0.095	Calibrated
$\mu_{S_2}^{X}$	Maximum specific growth rate of SRB *o*-xylene degraders (1/day)	0.022	Calibrated
μ_{S_3}	Maximum specific growth rate of IRB[b] ethanol degraders (1/day)	0.07	Calibrated
μ_{S_4}	Maximum specific growth rate of SRB ethanol degraders (1/day)	0.55	Calibrated
μ_{S_5}	Maximum specific growth rate of fermentative bacteria (1/day)	50	Calibrated
μ_{S_6}	Maximum specific growth rate of methanogenic archaea (1/day)	0.06	Calibrated
Y_{Fe}^{B}	Mass ratio of iron to benzene (-)	21.45	stoichiometry
Y_{Fe}^{T}	Mass ratio of iron to toluene (-)	21.83	stoichiometry
Y_{Fe}^{X}	Mass ratio of iron to *o*-xylene (-)	22.09	stoichiometry
Y_{Fe}^{EtOH}	Mass ratio of iron to ethanol (-)	14.54	stoichiometry
$Y_{Fe}^{CH_4}$	Mass ratio of iron to methane (-)	27.85	stoichiometry
$Y_{SO_4}^{B}$	Mass ratio of sulfate to benzene (-)	4.61	stoichiometry
$Y_{SO_4}^{T}$	Mass ratio of sulfate to toluene (-)	4.69	stoichiometry
$Y_{SO_4}^{X}$	Mass ratio of sulfate to *o*-xylene (-)	4.75	stoichiometry
$Y_{SO_4}^{EtOH}$	Mass ratio of sulfate to ethanol (-)	3.13	stoichiometry

Symbol	Definition	Value	Source
$Y_{SO_4}^{CH_4}$	Mass ratio of sulfate to methane (-)	5.99	stoichiometry
Y_{Acet}^{EtOH}	Mass ratio of acetate to ethanol (-)	1.3	stoichiometry
$Y_{CH_4}^{Acet}$	Mass ratio of methane to acetate (-)	0.27	stoichiometry
K_B	Benzene half-saturation concentration (mg/L)	0.5	Calibrated
K_T	Toluene half-saturation concentration (mg/L)	0.01	Calibrated
K_X	O-xylene half-saturation concentration (mg/L)	0.15	Calibrated
K_{EtOH}	Ethanol half-saturation concentration (mg/L)	1	Calibrated
K_{Acet}	Acetate half-saturation concentration (mg/L)	0.1	Calibrated
K_{Fe}	Iron half-saturation concentration (mg/L)	10	Calibrated
K_{SO4}	Sulfate half-saturation concentration (mg/L)	100	Calibrated
$K_{SO_4}^i$	Sulfate inhibition concentration (mg/L)	5	Calibrated
K_{Fe}^i	Iron inhibition concentration (mg/L)	2000	Calibrated
$Y_{S_2}^B$	SRB yield per benzene mass utilized (-)	0.015	[*Rittmann and McCarty*, 2001]
$Y_{S_2}^T$	SRB yield per toluene mass utilized (-)	0.014	[*Rittmann and McCarty*, 2001]
$Y_{S_2}^X$	SRB yield per *o*-xylene mass utilized (-)	0.014	[*Rittmann and McCarty*, 2001]
$Y_{S_3}^{EtOH}$	IRB yield per ethanol mass utilized (-)	0.053	[*Rittmann and McCarty*, 2001]
$Y_{S_4}^{EtOH}$	SRB yield per ethanol mass utilized (-)	0.015	Calibrated
$Y_{S_5}^{EtOH}$	Fermentative bacteria yield per ethanol mass utilized (-)	0.015	Calibrated
$Y_{S_6}^{Acet}$	Archaea yield per acetate mass utilized (-)	0.001	Calibrated
b_1	Decay rate of bacteria populations (1/day)	0.015	Calibrated
b_2	Decay rate of archaea (1/day)	0.01	Calibrated
f_{EtOH}	Ethanol threshold flag, set to 0 if ethanol is above the value listed at right, or 1 otherwise (mg/L)	1	[*Adair and Wilson*, 2012]
f_{SO4}	Sulfate threshold flag, set to 0 if sulfate is below the value listed at right, or 1 otherwise (mg/L)	15	

[a] SRB is short for sulfate-reducing bacteria.

[b] IRB is short for iron-reducing bacteria.